Pardo Pascual, JE.; Almonacid Caballer, J.; Ruiz Fernández, LÁ.; Palomar-Vázquez, J. (2012). Automatic extraction of shorelines from Landsat TM and ETM+ multi-temporal images with subpixel precision. Remote Sensing of Environment. 123:1-11. doi:10.1016/j.rse.2012.02.024.

Elsevier Editorial System(tm) for Remote Sensing of Environment
Manuscript Draft

Manuscript Number:

Title: Automatic Extraction of Shorelines from Landsat TM and ETM+ Multi-Temporal Images with SubPixel Precision

Article Type: Full length article

Keywords: shoreline subpixel detection; Landsat images; coastal processes; beach management

Corresponding Author: Dr Josep E Pardo-Pascual, PhD

Corresponding Author's Institution: Universidad Politecnica de Valencia

First Author: Josep E Pardo-Pascual, PhD

Order of Authors: Josep E Pardo-Pascual, PhD; Jaime Amonacid-Caballer, MD; Luis A Ruiz, PhD; Jesus Palomar-Vazquez, PhD

## Research Highlights

A sub-pixel automated shoreline detection method from images is presented > Errors are analysed using 45 Landsat TM and ETM+ images over microtidal coast > Modelisation of errors allows to improve precision in shoreline location > Mean error ranges from 1.22 to 1.63 m and RMSE from 4.69 to 5.47 m > The method can be used to analyse coastal evolution trends in large temporal series.

# Automatic Extraction of Shorelines from Landsat TM and ETM+ Multi-Temporal Images with SubPixel Precision

**Josep E. Pardo-Pascual [a*], Jaime Amonacid-Caballer [a], Luis A. Ruiz [a], Jesus Palomar-Vazquez [a]**

*[a]Geo-Environmental Cartography and Remote Sensing Group*
*Department of Cartographic Engineering, Geodesy and Photogrammetry*
*Universitat Politècnica de València.*
*Camí de Vera s/n, 46022 València, Spain*
*Corresponding author. Email: jepardo@cgf.upv.es*
*Phone: 34963877007 (Ext:75537); Fax: 34963877559*

## Abstract

A high geometric precision method for automated shoreline detection from Landsat TM and ETM+ imagery is presented. The methodology is based on the application of an algorithm that ensures accurate image geometric registration, and a new algorithm for sub-pixel shoreline extraction, both at sub-pixel level. The analysis of the initial errors shows the influence of the differences in reflectance of land cover types over the shoreline detection, allowing us to create a model to substantially reduce these errors. Three correction models were defined attending to the type of gain used in the acquisition of the original Landsat images. Error assessment tests were applied on three straight coast segments artificially stabilized, all of them located in microtidal coastal areas. A testing set of 45 images (28 TM, 10 ETM high-gain and 7 ETM low-gain) was used. The mean error obtained in shoreline location ranges from 1.22 to 1.63 m, and the RMSE from 4.69 to 5.47 m. Since the errors follow a normal distribution, then the maximum error at a given probability can be estimated. The results obtained show the possibility to apply this methodology over large coastal sectors in order to determine and analyse the evolution trend of these dynamic areas.

Keywords: shoreline subpixel detection, Landsat images, coastal processes, beach management.

## 1. Introduction

The recognition of changes in the position of the shore is crucial for understanding the dynamics of coastal areas and especially the shorelines. The position of the shore can change for two reasons: (i) more

33 or less predictable short-term variations in sea level that critically depend on astronomical and
34 meteorological factors (Lisitzin, 1974, Pugh 1996, 2004); and (ii) alterations in the shape and volume of
35 sediments along the profile of the shore. These morphological changes are much less predictable because
36 they are a response of the shore system to wave conditions.

37 Morphosedimentary changes to shorelines can be of two types: (a) those that occur in the short-term
38 (generally less than a year) and depend on whether the waves are pushing towards the land or sea; and (b)
39 longer-term changes that can be detected after several years and are caused by accumulation or erosion.

40 Both types of changes are important in the management of coastal areas (DGC, 2008) given that the first
41 type of change reveals the magnitude of the variability over the course of a year and so enables a coastal
42 management analyst to define and establish protected shore areas without worrying about specific
43 changes that may occur after, for example, a major storm. The second type of change reveals a definite
44 trend and is more important as it enables predictions to be made in the short or medium term about
45 whether the shore could witness significant changes that may prevent some uses, or endanger spaces
46 adjacent to the coast. On the Spanish Mediterranean coast, where a major tourism industry is established,
47 recognition of the meaning and speed of changes may be strategically important because such information
48 would enable corrective actions to be taken to avoid or minimise risk (Pérez-González, 2008).

49 For this reason it has been standard practice for many decades to track the position of the shore using
50 aerial photographs as the primary source (McCurdy, 1950; Stafford, 1971; MOPU, 1979; Leatherman,
51 1983; Smith and Zarrillo, 1990; Pardo-Pascual, 1991, Thieler & Danforth, 1994; Jiménez *et al.*, 1997).
52 On a coast with virtually no tides – such as much of the Mediterranean coast – the visual recognition of
53 the location of the shore from an aerial photograph is simple. The task is more complex in tidal areas
54 since the location of the shore at a given instant is much less likely to reveal changes or trends. Many
55 solutions have been proposed for this problem. Boak & Turner (2005) described up to 44 different
56 indicators of the location of the shore as used by different authors from the 1950s until today.

57 Satellite images have been seen as an extremely attractive option for monitoring shorelines. However,
58 few applications took advantage of the optical spectral range until high spatial resolution satellites
59 became available at the beginning of this century – as evidenced by a recent review by Gens (2010).
60 Methodological solutions since the early 90s have focused primarily on the use of SAR images (Lee &
61 Jurkevich, 1990, Mason and Davenport, 1996, Niedermeier *et al.*, 2000; Yu & Acton, 2004). More

recently, LiDAR technology has been the focus of most of applications by various authors and this has led to increased work on the definition of shorelines with reference to specific contour lines – such as the mean water height line – rather than other visual signs. This new approach can be used in tidal and non-tidal waters (Stockdon *et al.*, 2002; White & Wang, 2003; Robertson *et al.*, 2004; Morton *et al.*, 2005) and is highly accurate (Liu *et al.*, 2007). The information provided by the LiDAR or SAR images is especially useful because it enables a highly precise characterisation to be made of three dimensional processes that are difficult to describe using just two dimensions. Multispectral satellite imagery offers many advantages: such as a large number of data records, the provision of repeated images of a single place at different times, and the fact that virtually the entire planet is covered. As a result, multispectral imagery is potentially more useful than previous sources for recognising evolutionary trends in the medium and long-term. The Landsat images acquired by the TM and ETM + sensors on the Landsat 5 and 7 series are the largest useable database of medium resolution images for studying the dynamics of coastal areas. Morever, since 2008 the US Geological Service (USGS) has freely provided all archived Landsat images, together with the newly acquired Landsat 7 ETM + SLC-off and Landsat 5 TM images with less than 40 percent cloud cover – and thereby enabling free access to multiple images of the same sectors.

Until now this information has been relatively little used. This is because a 30 m spatial resolution is too coarse to detect most of the changes in the shoreline within the timescale required for coastal management (Pardo-Pascual & Sanjaume, 2001). However, several exceptions are worth mentioning and these are usually found in places such as deltas that show abrupt changes of great magnitude. Applications on the Nile delta (White & El-Asmar, 1999), the Maritsa delta on the Aegean coast of Turkey (Ekercin, 2007), or the Huanghe river (Yellow River) in China (Chu *et al.*, 2006) are good examples. Landsat images have also been used to map the various environments within tidal flats and describe the three-dimensional nature of these domains by determining the various shorelines (Ryu *et al.*, 2002). A similar goal is found in applications on coral reef atolls in the Marshall Islands (Yamano *et al.*, 2006) where the aim is to describe the topography of the intertidal zone. Landsat TM and ETM + images have also been used in various studies to build digital lines of complex coastal regions such as Louisiana (Braud & Feng, 1998); locate wetlands in flood plains (Frazier and Page, 2000); detect changes in reservoirs (Manavalan *et al.* 1997); or monitor natural lakes such as the Rift Valley in Kenya (Ouma and

Tateish, 2006). In all of these cases, it was assumed that the level of accuracy produced by mapping the shoreline would always be worse than the 30 m resolution of the original images.

There are many examples of automatic extraction of shorelines from high spatial resolution images, and some of these examples include: applications on the Ebro delta based on SPOT 3 (Rodriguez., 2001, Rodriguez *et al.,* 2009); an analysis of the Spanish Andalusian coast based on ASTER imagery (Espinosa and Rodriguez, 2009); or the Spanish Valencian coast using IRS-Pan images with a 5.6 m spatial resolution (Brocal *et al.* 2001; Brocal *et al.,* 2005); Ikonos images (Di *et al.,* 2003a, b); and QuickBird images (Pardo-Pascual *et al.,* 2008). The accuracy with which the shoreline was measured in all of these works is relative to the size of the pixel in the images used.

Much of the effort made so far by researchers has been focused on defining an optimal method to reliably locate the position of the shore. Many types of solution have been proposed – from the use of a supervised classification (Hoeke *et al.,* 2001, Pardo-Pascual *et al.,* 2008, Espinosa and Rodriguez, 2009); unsupervised classified images (Ekercin, 2007; Guariglia *et al.* 2006); and various thresholding techniques (White and El-Asmar, 1999; Jishuang and Chao, 2002; Yamayo *et al.* 2006; Bayram *et al.,* 2008, Maiti and Bhattacharya, 2009). In any of these methods each of the pixels will ultimately be considered as sea or land and this means they cannot be used to monitor small changes to the shoreline (<10 m) unless high resolution images are used. Foody *et al*. (2005) propose the use of fuzzy logic to resolve this limitation inasmuch as the same pixel can be assigned partially for the sea and partially for land. Muslim *et al. (*2006, 2007) have been presenting in successive publications improved solutions to accurately determine how much of each pixel should be assigned to each of these two regions. To facilitate the evaluation of the method the authors in these works began from an IKONOS image from which the actual position of the shore could be fixed. The same image is then degraded to dimensions similar to those of the SPOT 3 with a 20 m pixel size (Foody *et al.* 2005; Muslim *et al.,* 2006) or Landsat 30 m images. All of the tests have been conducted on a small 125 m section of the coast of Indonesia. The root mean square error (RMSE) of the shoreline predictions from the two-point histogram method – the method that obtains the best results – lays in the range 1.15-2.08 m and 1.71-5.11 m for imagery with a 16 and 32 m spatial resolution, respectively (Muslim *et al.,* 2007). While these results are extremely interesting, the fact that the tests have been performed on such small segments makes it difficult to assess whether they can be generally applied to wider areas. However, it is clear that only the subpixel approach

can detect the position of the shoreline from medium-resolution images with enough accuracy to be useful in coastal management.

However, an efficient subpixel level extraction procedure of the shoreline is required for the method to be applied to the series of Landsat images available since 1984, as well as a method to very accurately superimpose the successive images. The aim of this paper is to propose a methodology to extract shorelines from successive Landsat images of the same place and also determine the level of precision that can be achieved. To achieve this we propose an algorithm for the extraction of the shoreline with subpixel precision to enable successive geo-referencing between images of the same place with subpixel precision – and also establish a method for assessing the degree of accuracy. Tests previously carried out using the process of extracting the shoreline with subpixel accuracy (Foody *et al.*, 2005; Muslim *et al.*, 2006, 2007; Ruiz *et al.*, 2007; Pardo-Pascual *et al.*, 2008) used degraded high-resolution images to emulate medium resolution images – and Landsat images were not used. In this study, we work directly with Landsat images. This fact forces us to approach the question of how the result is affected by the type of image and the nature of the geography.

## 2. Study area

The study has focused on a section of the Spanish Mediterranean coast about 20 km in length that extends from the port of Castelló de la Plana and the immediate area of the port of Borriana (Fig. 1). It is a low-lying area formed on the coastal ends of two alluvial fans: the river Millars to the north and the river Anna to the south (Sanjaume *et al.* 1996). Until recently, the entire segment was mostly formed of pebble beaches – with sand beaches in some areas (Sanjaume, 1985) but the area has been extensively developed in recent years.

This is a microtidal coast and the average tidal range is less than 25 cm and the maximum positions of sea level over a year do not exceed 80 cm (Puertos del Estado, 2009). The average waves affecting the sector under study have relatively low energy levels (the average significant wave height is 0.7 m and the average peak wave period is 4.2 seconds). However, wave height during storms can reach up to 5 m and the peak period may extend to 15 seconds (wave data obtained from Spanish State Port Authority database*:* http://w3.puertos.es/es/oceanografia_y_meteorologia/banco_de_datos/oleaje.html*)*. Most of the

storms in the sector come from the northeast and given the general orientation of the coast the result is a drift that carries coastal sediment to the south. Serra-Peris (1986) estimates a potential net southerly movement of 590,000 $m^3$ annually. The construction of breakwaters at the ports of Borriana and Castelló de la Plana have disrupted this longitudinal movement and caused a major accumulation of sediments in the north and significant erosion in the south (Pardo-Pascual, 1991; Sanjaume & Pardo-Pascual, 2005). Artificial rock seawalls have been built over the past 50 years to stop such erosion around the downdrift piers and so stabilise the shoreline. In fact, some 11 km of 20 km of the surveyed shoreline have been artificially protected with rock seawalls (Fig. 1).

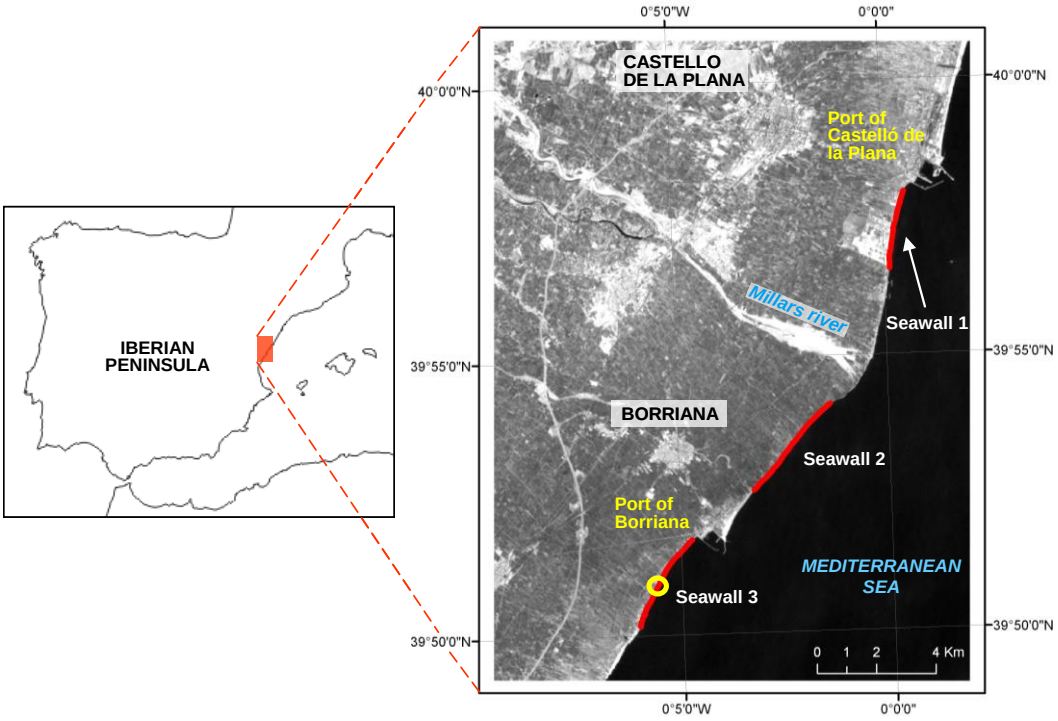


Figure 1. Seawalls in the study area.

The fact that this part of the shoreline has been artificially stabilised is precisely why we have chosen this area for study. Our aim is to establish the level of accuracy that can be achieved in determining the position of the water line and, therefore, we have sought areas in which we can be sure that no changes have occurred in the position of the shore during the period of analysis (1984-2010).

The analyses were focused on three coastal segments that during the period 1984-2010 were always artificially stabilised. The first segment, termed Seawall 1, is located immediately south of the port of Castelló de la Plana and extends 2.9 km. The port of Castellón was expanded after 2005 and a part of this breakwater was immersed in the port. Industrial facilities have been built on the coast and there are small

166 installations such as piers and loading points. As a result, the shoreline is not completely straight and
167 appears curved in some places (an example can be seen in Figure 9). The second segment – termed
168 Seawall 2 – is 2.4 km long and straight. Farmland borders the shoreline (Fig. 7). The third segment is
169 2.73 km long and starts immediately south of the docks at Borriana. The shoreline is also straight and the
170 adjacent land is urban in the north and farmland to the south. Importantly, in 2005 a detached groin was
171 built and this has enabled the creation of a small beach (indicated with a circle in Figure 1).

172

173 # 3. Data

174 All images used are taken from the USGS database at: http://edcsns17.cr.usgs.gov/NewEarthExplorer/
175 and are catalogued by the Landsat program as L1T product (NASA, 2006). This product is georeferenced
176 with a level of precision that is always better than 0.44 pixels (meaning 13.4 m). The images have been
177 resampled using a cubic convolution method. Images have been taken using the TM (Landsat 5) and
178 ETM + (Landsat 7) sensors. The radiance ranges are homogeneous for images acquired with the Landsat
179 5 TM sensor; but the images taken with the Landsat 7 ETM + sensors may reveal high or low gain.

180 We have worked with 45 images (see Table 1) corresponding to the 199-032 scene and covering the
181 period September 1984 to July 2010.

182 Table 1. Characteristics of images analysed. The image type column distinguishes between images taken
183 by the TM sensor and those taken with the ETM high gain (ETM-H) and ETM low gain (ETM-L).

| Date | Type | Date | Type |
|---|---|---|---|
| 1984.09.21 | TM | 2002.04.24 | ETM-H |
| 1984.10.07 | TM | 2002.05.26 | ETM-L |
| 1984.10.23 | TM | 2002.06.19 | TM |
| 1984.11.24 | TM | 2002.07.29 | ETM-L |
| 1986.05.22 | TM | 2002.08.30 | ETM-L |
| 1986.06.23 | TM | 2003.02.06 | ETM-L |
| 1986.08.10 | TM | 2003.03.10 | ETM-L |
| 1986.08.26 | TM | 2003.04.27 | ETM-L |
| 1986.10.29 | TM | 2003.05.29 | ETM-L |
| 1987.04.23 | TM | 2003.07.08 | TM |
| 1987.06.26 | TM | 2003.08.25 | TM |
| 1987.07.12 | TM | 2007.01.24 | TM |
| 1987.08.13 | TM | 2007.02.09 | TM |
| 1990.09.06 | TM | 2007.03.13 | TM |
| 1999.07.21 | ETM-H | 2007.08.04 | TM |
| 2000.01.29 | ETM-H | 2007.08.20 | TM |
| 2000.03.01 | ETM-H | 2009.06.22 | TM |
| 2000.08.08 | ETM-H | 2009.07.24 | TM |

| | | | |
|---|---|---|---|
| 2000.09.09 | ETM-H | 2009.08.09 | TM |
| 2000.10.27 | ETM-H | 2009.09.10 | TM |
| 2001.07.26 | ETM-H | 2009.10.12 | TM |
| 2001.10.30 | ETM-H | 2010.07.27 | TM |
| 2002.02.19 | ETM-H | | |

184

185 The distance and angle of each point was measured with regard to the actual position of the coastline in
186 order to calibrate the accuracy with which the different shorelines can be obtained after applying the
187 algorithm. To set the real position of the shoreline in the area near the seawalls, the positions were
188 digitised from a series of aerial photos taken in July 2006 as part of the National Program for Aerial
189 Orthophotography (PNOA in Spanish). These aerial photos have a spatial resolution of 0.5 m/pixel and
190 use three spectral bands (IR, R, G). The digitisation of the shoreline was performed over a screen image
191 at a scale of 1/2000 with an estimated error of ± 1 m. The uncertainty in the reference position of the
192 shoreline is estimated at ± 1.3 m. These same aerial photos have been used as base material for
193 georeferencing at subpixel level (as explained in paragraph 4.1).

194 # 4. Methodology

195 In this section the method for registering images at subpixel level is described in detail; an automatic
196 algorithm for the extraction of the shoreline is proposed; and the specific way in which the methodology
197 has been applied to Landsat images is also explained.

198 ## *4.1 Geo-referencing at subpixel level*

199 NASA has geo-referenced the Landsat images with great precision (better than 0.4 pixels) but given the
200 objectives proposed in this paper, it was considered necessary to determine the variation in position
201 between successive images at a subpixel level. This was achieved by applying a single-step discrete
202 Fourier transform (DFT) algorithm (Guizar-Sicairos et al., 2008). This algorithm is based on the use of
203 cross-correlation within the space of the frequencies of two overlapped images. The single-step DFT
204 method is based on increasing the resolution of the original image (increased by a factor of *k)* and so
205 providing spectral information of the original image. Given the Fourier transformation of an image, it is
206 possible to 'embed' these frequency values in a matrix of zeros. The inverse transformation will have the
207 dimensions of the new matrix with the spectral information of the original image. The cross-correlation
208 localises the maximum correlation peak at a higher resolution than the original image and so the

displacement can be measured with sub-pixel accuracy. A precision of 1/k pixels is obtained – depending on the k factor of the increase applied.

This method determines the magnitude of displacement on the *x* and *y* axes when comparing two images of the same place. This is achieved without using ground control points. In our case, given that we aim to achieve highly accurate geo-referencing, a mosaic of IR band aerial photographs with a resolution of 0.5 m is taken as reference. This mosaic has been degraded to a resolution of 30 m in order to produce the same pixel size as the Landsat TM images. Subsequently, we applied the single-step DFT algorithm with which it is possible to calculate the amount of displacement for *x* and *y* in each image in comparison with the aerial photographs degraded to 30 m per pixel. Table 2 shows the displacements applied to register successive images at subpixel level. It can be seen that we are dealing with relatively small variations – the average being 2.4 m for both *x* and *y* axes. Nevertheless, these steps are necessary to achieve the maximum accuracy in the process of extracting results.

### *4.2. Automatic extraction of the shoreline at subpixel level*

The proposed method is based on the different spectral response of water and land, especially in the infrared bands – and the fact that the shoreline under study tends to have a homogenous shape. Based on these circumstances, the developed algorithm attempts to approximate the most likely position of the shoreline (or the separation between water and land). The algorithm has been developed in two phases: in the first phase a line is extracted at the pixel scale (Figure 2); and in the second phase a new position based on the initial line is calculated at subpixel level.

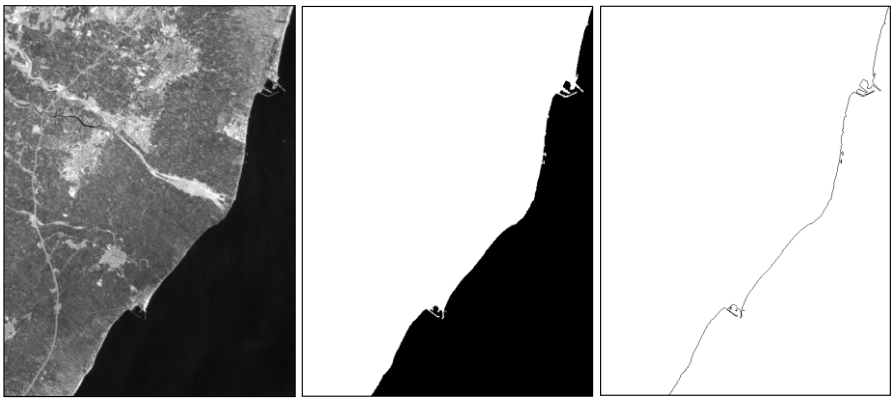

Figure 2. The figure illustrates the scheme of the first phase: an approximation of the positioning of the coast at pixel level.

In the first phase an approximation based on a binarisation of the original image is obtained by determining the best threshold for distinguishing the two areas in the infrared image. A significant sample of the areas of sea and land is made and the histograms are studied. It is assumed that both histograms show a normal distribution, and this enables a characterisation to be made using the average parameters and standard deviation. The point of intersection between the two distributions (Fig. 2) is modeled and automatically determined. This thresholding requires post-filtering since there are often pixels or small areas on the land that are confused as sea. To address these small areas, the land area is bounded and made solid. In general, the sea is correctly defined by the initial thresholding. Once the correction has been made the land area is dilated and the previous thresholding is subtracted. While this process may move the line one pixel towards the sea, this effect will have no practical significance because the line is only used to approximately define the neighbourhood in the subsequent analysis.

Once the approximate line of separation between the land and sea has been obtained, the next step is to extract the position of the shoreline at subpixel level. The assumption underlying the algorithm is that the real separation between water and land will be where the gradient of digital levels on an infrared image is greatest. As the aim is to locate this border at a level of detail greater than a pixel; the proposed solution is to calculate the position on a mathematically modelled surface (enabling any desired level of detail to be achieved) which has been produced from data provided by the infrared image. Accordingly, a mathematical function is adjusted to model this sudden change in the spectral response at the interface of water and land in the neighbourhood of the approximate line that was initially obtained (Fig. 3). To achieve this we studied various options and eventually selected a robust solution consisting of adjusting by least squares with a fifth order polynomial. For this approach it was necessary to initially resample the original image by a factor of four using bicubic interpolation, and then make adjustments on a sufficiently large area of the image (applied on a 7x7 neighbourhood of pixels around each pixel of the approximate line).

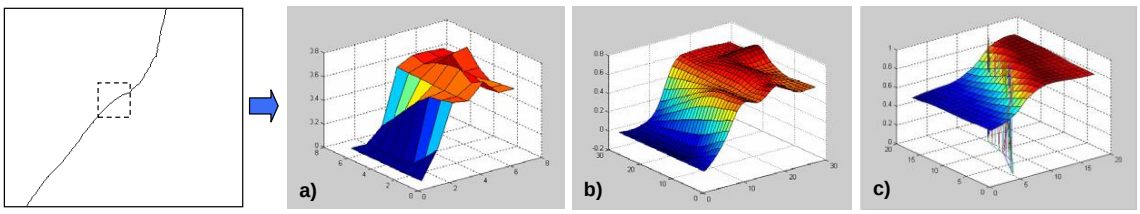

Figure 3. Basic scheme of the calculation procedure for the shoreline position: a) the neighbouring pixels of the approximate line are selected; b) resampling is performed to produce a greater density of points for the mathematical function; c) the function and its line of inflection is mathematically obtained.

Once a suitable mathematical function is obtained the position in the gradient where the perpendicular direction to the initial line is maximum is analytically determined – and points corresponding to the shoreline for each iteration are established. The position of the maximum gradient is determined by performing successive profiles on each of the resampled pixels in the image. Thus, after resampling an image with a resolution of 30 m a profile is obtained for approximately every 7.5 m. Since the process is performed for each pixel in the approximate line and a 7x7 neighbourhood is used, the same pixel is usually processed in several neighbourhoods, so that each time the neighbourhood is changed the function changes and different positions are calculated for each approximation – producing in this way seven solutions for each given position. The final position is determined by a weighted averaging of the seven defined positions. Figure 4 shows the approximate line in blue; and the different solutions in white for each neighbourhood that has included the pixel; and finally, the line shown in yellow is obtained by averaging the position of the lines from these neighbourhoods.

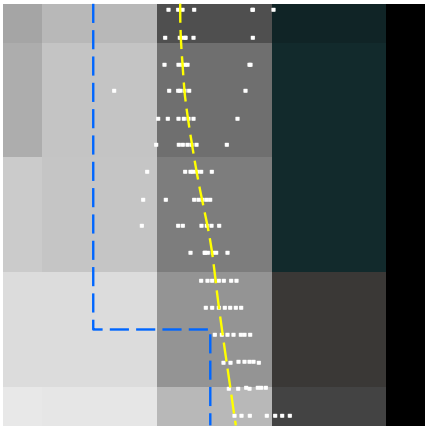

Figure 4. Approximate line at pixel level (in blue); the white dots show the calculations made for each analysed profile; and the yellow line indicates the averaged position of the multiple solutions determined by the various profiles and the calculated shoreline.

This algorithm was initially tested on high-resolution images (QuickBird) resampled to 28.8 m to simulate the approximate resolution of Landsat TM images; and the results were compared with the position previously extracted using the original image in the panchromatic band (with a resolution of 0.6 m). When this method was applied on a segment of about 11 km of sandy beach with almost no tide (using a QuickBird infrared band image taken on 17 November 2004) and re-sampled to 28.8 m, an mean error in the position of -3.98 m (negative value indicates the prevalence of landward errors) and a

282 standard deviation of 4 m was obtained. These results suggest the possibility of extracting from Landsat
283 data the position of the shoreline with sufficient precision to recognise seasonal variability and annual
284 trends.

285 ### *4.3. Use of Landsat images, selection of the optimum band, and evaluation method*

286 The method has been applied on *tiles* of 1000 x 1000 pixels from Landsat (199-032) so that the algorithm
287 could be more efficiently managed. To extract the shoreline before applying the algorithm, the image was
288 normalised according to the maximum and minimum in order to avoid large differences that could reduce
289 the consistency of the method. After applying the algorithm to extract the shoreline, a series of successive
290 points are obtained. The x and y movements reflect the calculations made during subpixel geo-
291 referencing. The final result is a series of points indicating the shoreline and spaced about 7.5 m apart
292 along the coast (Fig. 5).


293

294 Figure 5. Example of the result for a segment of shoreline that has been artificially stabilised. Yellow dots
295 show the position of the shoreline image obtained from Landsat 5 (2000-03-01). The red line shows the
296 reference shoreline taken from the aerial photo with an underlying resolution of 0.5 m.

297 To assess the general validity of the results, the minimum distance to the reference shoreline was
298 measured – given that this distance represents the error at each point. This error could have a positive
299 value (if the point is found seaward of its true position) or negative (if found landward). Analyses were
300 always performed on areas where it was certain that no change had occurred during the study period.

301 The near-IR bands theoretically reveal a greater change in reflectance between the sea and land. Tests
302 were conducted on seven images to select the optimum spectral band. It was observed that in band 5 in
303 six of the tests, the mean error (about 1.3 m on average) and the standard deviation (0.75 m on average)
304 were lower than those obtained with band 4. These results are consistent with those observed by other
305 authors (such as Frazier & Page, 2000) who found fewer errors in determining the position of wetlands
306 when thresholding on band 5 in comparison with bands 4 and 7. Based on these results it was decided to
307 perform the rest of the analysis only on band 5.

308 Initial tests were conducted on a set of 23 images that were geo-referenced at subpixel level and then the
309 algorithm to extract the shoreline was applied. Once the 23 shorelines were extracted the differences were
310 evaluated between the position calculated using Landsat imagery and the reference shoreline. To test the
311 validity of the proposed method, the three segments of the reference shoreline included three artificially
312 stabilised seawalls (8026 m in length) that were in existence during the entire period for which images are
313 available.

314 When assessing the robustness of the method it is important to determine whether the magnitude and
315 direction of the errors are homogeneous in space and time and with the various types of Landsat images.
316 To evaluate the temporal response it was ensured that the 23 images covered the 26 years between 1984
317 and 2010 (Table 2). To analyse the possible spatial differences, assessment tests were made on three
318 segments of seawalls in the area. The seawalls were similarly sized but had substantial differences in the
319 landside surface covering, which generated significant differences in spectral response that may have
320 affected the efficiency of the method. To evaluate the response according to the type of image, a
321 differentiation of the images into three basic types was made according to radiance gain: those taken with
322 the TM sensor; those taken with the ETM+ high gain sensor (ETM-H); and those taken with the ETM+
323 low gain sensor (ETM-L).

## 324 **5.** Initial results and error analysis

325 Table 2 presents a summary of the error statistics obtained for each of the dates analysed and Figure 6
326 shows the mean error recorded over time. The table shows the number of points for which the error has
327 been checked, as well as the maximum seaward deviation,and the maximum landward deviation. The
328 mean error is obtained by averaging all the errors and interpreting the level of bias toward land or sea.
329 Finally, the standard deviation indicates the variability around the mean error.

Table 2. Shows the application of subpixel geometric correction and a summary of errors found after applying the geometric correction and the algorithm to Landsat images. The error values are in meters. Columns d (*x*) and d (*y*) show the displacement in *xy* applied after geometric correction.

| Date | d x (m) | d y (m) | Type | Maximun error | | Mean error | SD |
|---|---|---|---|---|---|---|---|
| | | | | Landward | Seaward | | |
| 1984.09.21 | -2.91 | -2.7 | TM | -25.41 | 27.15 | 5.42 | 8.05 |
| 1984.10.07 | -2.61 | -3.75 | TM | -19.27 | 32.75 | 6.71 | 8.01 |
| 1984.10.23 | -4.17 | -2.52 | TM | -22.9 | 33.68 | 8.34 | 8.23 |
| 1984.11.24 | -4.32 | -2.58 | TM | -13.21 | 29.83 | 8.34 | 7.67 |
| 1986.05.22 | -0.48 | -3.72 | TM | -20.44 | 30.24 | 7.03 | 7.4 |
| 1986.06.23 | -1.14 | -3.54 | TM | -24.47 | 23.81 | 5.74 | 7.26 |
| 1986.08.26 | -3.45 | -3.12 | TM | -19.61 | 24.84 | 6.38 | 7.21 |
| 1986.10.29 | -4.2 | -1.89 | TM | -21.38 | 33.01 | 8.71 | 7.37 |
| 1987.04.23 | -1.65 | -4.14 | TM | -59.69 | 25.04 | 6.04 | 6.69 |
| 1987.06.26 | -2.82 | -3.54 | TM | -20.23 | 28.49 | 5.68 | 6.76 |
| 2000.08.08 | -4.41 | -4.95 | ETM-H | -17.01 | 29.57 | 1.34 | 7.67 |
| 2000.09.09 | 0.84 | -3.84 | ETM-H | -21.42 | 27.43 | 1.7 | 7.61 |
| 2000.10.27 | -1.68 | -0.87 | ETM-H | -23.18 | 27.87 | 7.19 | 7.08 |
| 2001.07.26 | -3.24 | -1.17 | ETM-H | -22.55 | 33.45 | 2.62 | 7.88 |
| 2001.10.30 | -1.8 | -0.09 | ETM-H | -17.41 | 32.16 | 5.67 | 8.26 |
| 2002.02.19 | -0.72 | -1.08 | ETM-H | -24.82 | 36.75 | 5.21 | 8.28 |
| 2002.04.24 | 1.17 | -2.49 | ETM-H | -14.35 | 39.21 | 2.52 | 6.91 |
| 2002.07.29 | -1.05 | -1.83 | ETM-L | -26.78 | 20.03 | 0.78 | 6.71 |
| 2002.08.30 | -2.7 | -1.56 | ETM-L | -32.34 | 23.39 | 1.42 | 7.15 |
| 2003.02.06 | -6.21 | 0.12 | ETM-L | -41.48 | 30.83 | 2.72 | 8.88 |
| 2003.04.27 | -0.03 | 0.51 | ETM-L | -25.48 | 38.64 | 2.57 | 7.75 |
| 2003.05.29 | -0.45 | -6.45 | ETM-L | -26.76 | 24.22 | 2.56 | 8.19 |
| 2010.07.27 | -4.23 | 0.51 | TM | -22.63 | 17.03 | 1.15 | 6.42 |

Analysis of these results shows that the mean error in all cases is positive – meaning that the applied method biases the position in a seaward direction. It can also be seen that the magnitude of the mean error is substantially higher for the TM image sensor than those produced by the more recent ETM + sensor (Fig. 6). However, an exception is the image taken in 2010 (taken with the TM sensor) which has a mean error of 1.15 m. Images taken before the 90s reveal anmean error ranging between 5.5 and 9 m.

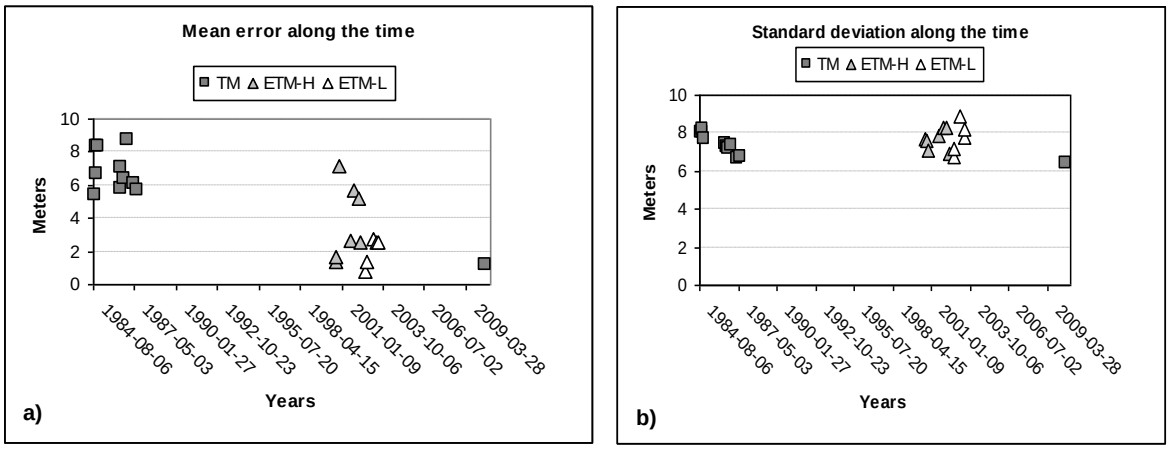


339

340 Fig. 6. Mean error (a) and standard deviation detected (b) expressed in meters for each image according to
341 the date when the image was taken and type of image.

342

343 Figure 6 shows that for TM and ETM-H images the mean errors reveal a significant homogeneity
344 between nearby dates. This suggests the possibility that changes in the type of land coverage are
345 influencing the positioning of the shoreline. Figure 7 (a) shows that in a small sector there are two
346 families of shorelines, one corresponding to images taken before March 2002 in which the shore is
347 located about 16 m seaward, while in images taken after April 2002 the shore is located about 22 m
348 landward. By comparing the images of February and April 2002 it can be seen that a major
349 transformation in plant cover had occurred in the adjacent area. The natural vegetation was eliminated and
350 the fields were ploughed – thereby causing a substantial change in the spectral response of the land. As a
351 result, these differences in reflectance affected the algorithm performance.

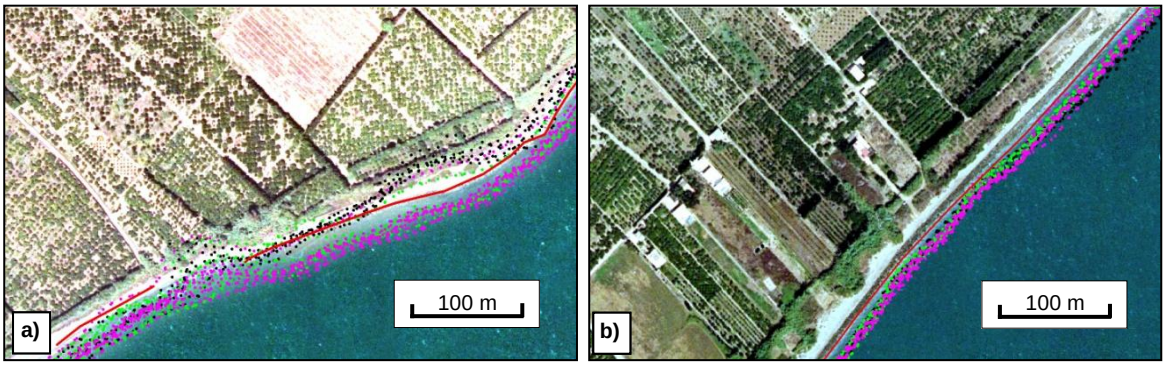


352

353 Fig. 7 Examples of error. In (a) it can be seen that there are two families of shorelines (see explanation in
354 the text) that appear to be related to a change in the landscape that significantly affected the intensity
355 value (IV) the land. In (b) it can be seen that in this sector for all of the period studied the error was
356 homogenous and the variability between the 23 shorelines was minimal.

357

Analysis of the standard deviations for the three types of images (Fig. 6b) shows that they have very similar values (ranging between 7.3 and 7.7 m). This enables us to conclude, firstly, that the way in which the shoreline is detected is usually quite robust – meaning that it is constant and the standard deviation is around 25% of the size of a pixel. A typical example is shown in Figure 7 b where the type of error detected in the 23 images analysed is usually the same: an error of about 12 m seaward.

An analysis of errors for each of the seawalls (Fig. 8b) shows that in every case Seawall 2 had a mean error that was significantly higher and clearly different to the errors seen for the other two seawalls. The size of this error on Seawall 2 is quite high – about 12 m for the TM images – and represents about 40% of the pixel size. Images taken with the ETM + sensor also clearly reveal a higher error for Seawall 2, although the error at 32% of a pixel is slightly lower than that obtained with TM images. Although the errors in the ETM-L images for Seawall 2 were also higher than the other seawall images they were less than 20% of pixel size. The magnitude of the mean errors for Seawalls 1 and 3 was substantially less in all cases – and in some cases near zero.

Error variability (Fig. 8b) as indicated by standard deviations is fairly homogeneous, although Seawall 3 shows minimum values of about 4 m while the other two seawalls are between 7 m and 9.6 m. It is noteworthy that Seawall 1 shows standard deviation values similar to or greater than those seen in Seawall 2, while the mean error was substantially higher in Seawall 2. What could explain this increased error variability in a sector despite the fact that the mean error is low?

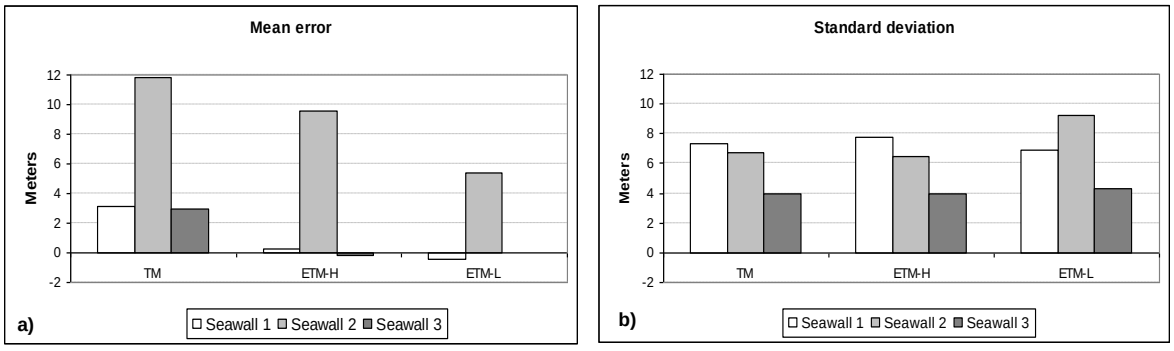


Fig. 8 Mean error (a) and standard deviation (b) for each of the three seawalls

The probable explanation is that there are curves in the shoreline near Seawall 1 due to the existence of small piers and this made modelling the land-water transition more difficult. Figure 9 reveals how alongside the sudden curves in the shoreline the algorithm shifts the calculated position of the shoreline some tens of meters to the north or south of the curve. This response of the algorithm can be explained if

we remember that the mathematical function is based on a 7 x 7 neighbourhood. Despite being fifth order, this function cannot directly adapt to such abrupt curves in the shoreline. However, if higher-level functions are used then false details are detected and unrealistic final lines are generated. We can conclude that this type of error is inherent to the method and therefore unavoidable.


Fig. 9. Example of localisation around Seawall 1. Evidence from these results suggests that the mathematical model for the extraction of the shoreline based on Landsat images usually works fairly well. However, errors are produced that seem to be directly related to the characteristics of the digital levels with which the extraction algorithm operates – meaning the 7 x 7 pixel neighbourhood.

A systematic analysis of the errors found after applying the algorithm and the geometric correction enables us to calculate that there are at least two types of errors affecting the outcome. One is the limitation of the method when detecting the shoreline in places where there are significant curves. As a result, this tool is only useful when applied to shores that are basically homogeneous – or when applied to stretches of shore that are straight for at least 210 m (or 7 pixels).

The second type of error results from how the positioning of the shoreline is affected by differences in the type of land cover. Figure 10 shows the relationship between the error in the positioning of the shoreline and two variables that describe the signal recorded in the image: the arithmetic mean of intensity values analysed in the neighbourhood of the 7x7 square of pixels used during the process of calculating the position of the shoreline; and the standard deviation of these digital levels. It can be seen that there is a clear relationship between the two variables; but neither, by themselves, can explain all the errors. The

403 fact, however, that both variables can be measured on the images suggests that it may be possible to
404 model the errors and so establish a system for correcting the described method.

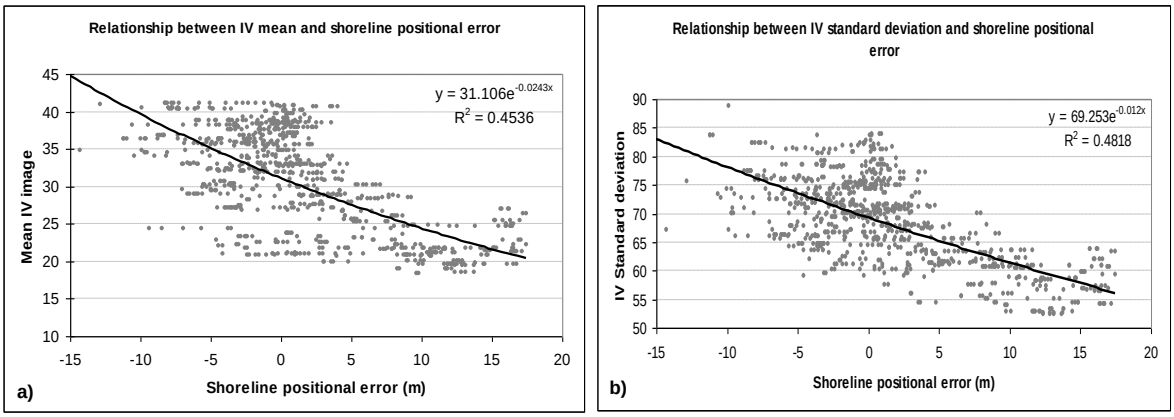


405

406 Fig. 10 (a) Relationship between the mean pixel intensity considered in the analysis and the error in the
407 positioning of the shoreline in areas near seawalls. (b) shows the relationship between the standard
408 deviation of the pixel intensity values (IV) in the analysis and errors. In both cases, the relationship shown
409 is found on the 199-032 series of images taken by the ETM + high gain sensor (21 July 1999).

410

411 # 6. Modelisation of the error and an improvement to the proposed

412 # algorithm

413 The bias that these factors cause in the error has been modelled after studying the characteristics of the
414 image, the mean and standard deviation of the intensity values of the pixels, and the error in the
415 positioning of the shoreline. A sufficiently large sample has been selected that does not contain other
416 known sources of error. Accordingly, we have chosen a significant and representative set of points
417 extracted using the described method – specifically five TM images, seven ETM-H images, and five
418 ETM-L images (see Table 4). These images include Seawalls 2 and 3 and the error has been linked with
419 the mean pixel intensity and standard deviation of the neighbourhood – analysed using multiple
420 regression for the location of each point. Because the image type (TM, ETM-H, ETM-L) affects the
421 magnitude of the error, a specific model has been defined for each type of image. Below are the error
422 adjustment functions for the three types of processed images, while Table 5 shows the results of the
423 adjustment.

424

***Error TM (E_TM)****= 30.1399 – 1.54981Mean^0 * STD^1 + 0.0135352 * Mean^0 * STD^2 +*

*0.251876*Mean^1*STD^0 + 0.00551167*Mean^1*STD^1 - 0.00456379*Mean^2*STD^0* (1)

***Error ETM+High gain (E_ETM-H)*** *= 24.3029 - 1.57048*MEAN^0*STD^1 + 0.0123342 * MEAN^0*

**STD^2 + 0.482115 * MEAN^1*STD^0 + 0.00129427*MEAN^1*STD^1 - 0.00351943 * MEAN^2 **

*STD^0* (2)

***Error ETM+-Low gain (E_ETM-L)****= 10.8645 - 1.20851 * MEAN^0 * STD^1 - 0.017857 * MEAN^0 **

*STD^2 + 0.824386 * MEAN^1 * STD^0 + 0.0362686 * MEAN^1*STD^1 - 0.0216562 * MEAN^2 **

*STD^0* (3)

Table 3. Basic statistics of the models obtained for the three types of images

| | R2 | Standard error estimate | Mean absolute error | Confidence level |
|---|---|---|---|---|
| E_TM | 0.45 | 5.34 | 4.03 | 99% |
| E_ETM-H | 0.58 | 4.71 | 3.56 | 99% |
| E_ETM-L | 0.33 | 6.28 | 4.72 | 99% |

The statistical models obtained are shown in Table 3 and reveal substantial improvement in the results given that the mean absolute error (meaning the average value of the residues) oscillates between 3.5 and 4.7 m; and the standard estimate error (which shows the standard deviation of the residues) ranges from 4.71 to 6.28 m. Logically, the models that show a better fit reveal lower mean absolute errors and so a substantial improvement in the positioning of the shoreline is to be expected, especially for ETM-H images and a little less so for the ETM-L images.

The error adjustment functions have been used to correct the positions according to the characteristics of the images. Table 4 shows the statistical errors for each image recorded before and after the bias correction and resulting from differences in the reflectance caused by differing land uses. The table also includes images used to define the correction models.

Table 4. Comparison of errors when using the algorithm in its original form and with the improvements after correcting for the effect associated with the characteristics of the image. The column *Model* indicates whether the image was used or not to define the applied correction models.

| Date | Type | First method | | | | Model | Improved Method | | | |
|---|---|---|---|---|---|---|---|---|---|---|
| | | Maximum Error | | Mean error | SD | | Maximum Error | | Mean error | SD |
| | | Landward | Seaward | | | | Landward | Seaward | | |
| 84.09.21 | TM | -25.41 | 27.15 | 5.42 | 8.05 | yes | -19.03 | 18.24 | 1.14 | 6.32 |
| 84.10.07 | TM | -19.27 | 32.75 | 6.71 | 8.01 | no | -23.05 | 24.71 | 2.58 | 6.15 |

| | | | | | | | | | | |
|---|---|---|---|---|---|---|---|---|---|---|
| 84.10.23 | TM | -22.9 | 33.68 | 8.34 | 8.23 | no | -21.23 | 19.82 | -1.25 | 5.01 |
| 84.11.24 | TM | -13.21 | 29.83 | 8.34 | 7.67 | yes | -19.26 | 25.23 | 0.79 | 5.31 |
| 86.05.22 | TM | -20.44 | 30.24 | 7.03 | 7.4 | yes | -19.38 | 19.45 | 3.30 | 5.80 |
| 86.06.23 | TM | -24.47 | 23.81 | 5.74 | 7.26 | yes | -18.15 | 19.02 | 2.73 | 5.47 |
| 86.08.26 | TM | -19.61 | 24.84 | 6.38 | 7.21 | yes | -16.89 | 19.80 | 3.46 | 5.68 |
| 86.10.29 | TM | -21.38 | 33.01 | 8.71 | 7.37 | no | -14.80 | 17.55 | 2.31 | 4.63 |
| 87.04.23 | TM | -59.69 | 25.04 | 6.04 | 6.69 | no | -15.31 | 15.69 | -1.57 | 4.85 |
| 87.06.26 | TM | -20.23 | 28.49 | 5.68 | 6.76 | no | -14.65 | 26.18 | 2.36 | 4.66 |
| 99.07.21 | ETM-H | -19.95 | 32.05 | 0.67 | 7.13 | no | -19.80 | 18.14 | 0.11 | 5.00 |
| 00.01.29 | ETM-H | -13.35 | 27.10 | 7.83 | 7.51 | no | -18.62 | 24.98 | 0.48 | 5.74 |
| 00.03.01 | ETM-H | -13.42 | 30.70 | 3.96 | 7.36 | no | -17.21 | 27.32 | 0.62 | 5.13 |
| 00.07.26 | ETM-H | -21.79 | 27.94 | 1.76 | 7.37 | yes | -18.04 | 19.16 | 2.59 | 5.79 |
| 00.08.08 | ETM-H | -17.01 | 29.57 | 1.34 | 7.67 | yes | -19.61 | 19.85 | 1.16 | 5.18 |
| 00.09.09 | ETM-H | -21.42 | 27.43 | 1.7 | 7.61 | yes | -19.75 | 17.15 | -2.78 | 4.92 |
| 00.10.27 | ETM-H | -23.18 | 27.87 | 7.19 | 7.08 | yes | -19.74 | 19.78 | -0.38 | 4.62 |
| 01.07.26 | ETM-H | -22.55 | 33.45 | 2.62 | 7.88 | yes | -19.65 | 19.96 | -1.36 | 5.63 |
| 01.10.30 | ETM-H | -17.41 | 32.16 | 5.67 | 8.26 | yes | -19.96 | 17.76 | 1.24 | 5.12 |
| 02.02.19 | ETM-H | -24.82 | 36.75 | 5.21 | 8.28 | yes | -16.59 | 19.69 | 0.01 | 4.83 |
| 02.04.24 | ETM-H | -14.35 | 39.21 | 2.52 | 6.91 | no | -23.95 | 30.32 | 1.46 | 5.72 |
| 02.07.29 | ETM-L | -26.78 | 20.03 | 0.78 | 6.71 | yes | -28.18 | 24.99 | -1.65 | 5.72 |
| 02.08.30 | ETM-L | -32.34 | 23.39 | 1.42 | 7.15 | yes | -26.02 | 27.33 | 2.65 | 6.58 |
| 03.02.06 | ETM-L | -41.48 | 30.83 | 2.72 | 8.88 | yes | -45.55 | 24.78 | 1.01 | 7.49 |
| 03.04.27 | ETM-L | -25.48 | 38.64 | 2.57 | 7.75 | no | -33.55 | 13.09 | -1.54 | 5.88 |
| 03.05.29 | ETM-L | -26.76 | 24.22 | 2.56 | 8.19 | yes | -22.53 | 29.74 | 2.39 | 5.61 |
| 03.05.29 | ETM-L | -26.76 | 24.21 | 2.56 | 8.18 | yes | -26.57 | 28.90 | 0.29 | 6.52 |
| 10.07.27 | TM | -22.63 | 17.03 | 1.15 | 6.42 | no | -21.46 | 11.02 | -1.32 | 5.14 |

A comparison of the first method with the second method shows how the movement of the mean error towards the sea has been stopped and the errors are now centred on zero – see Figure 11a. As a result, the magnitude of the errors in all cases is reduced to around 3.5 m. The mean error before applying the described method was 4.6 m, and this error has now been reduced to 0.8 m. It is also worthwhile noting that the errors in the improved solution are basically stable over time, and are not especially affected by the type of image used. This can be seen clearly by comparing Figure 11a and Figure 6a..

The standard error deviations have also improved. A comparison of Figure 11b and Figure 6b shows that errors are now between 4.7 m and 7.4 m. Interestingly, TM and ETM-H images reveal very similar deviations. However, the ETM-L errors are slightly greater. Another indication of the greater scatter in the data produced with the ETM-L images (in comparison with other two types of images) is given by an analysis of maximum and minimum errors: while the TM and ETM-H show an average minimum and maximum error of -18.5 m and 20.0 m; while for ETM-L the figures are -29.5 m and 25.6.

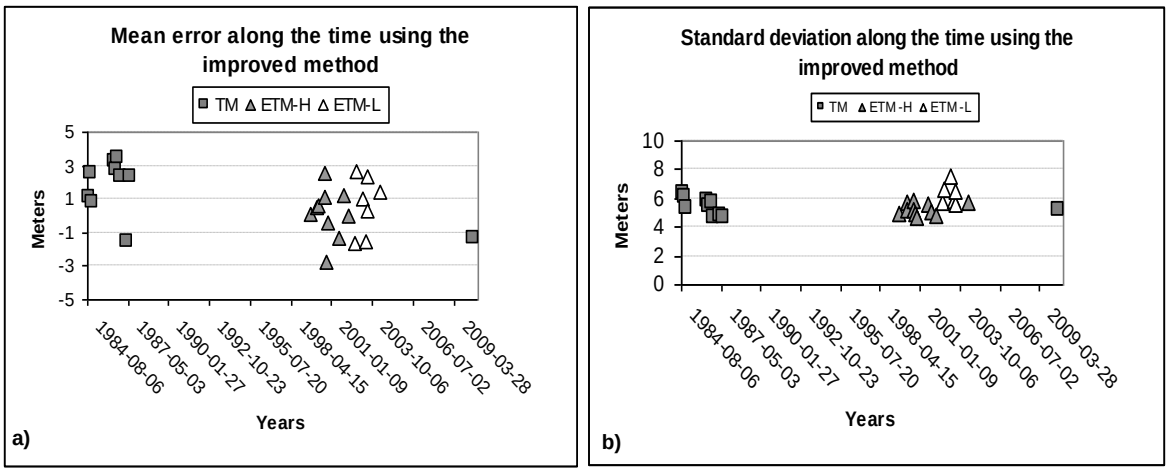


461

462 Fig. 11. Mean error and standard deviation of the error after applying the improved method.

463

464 As previously mentioned, to define the models of correction for differences in reflectance a small number
465 of images were used (5 for TM, 7 for ETM-H, 5 for ETM-L) and so it is worth asking if the model can be
466 extrapolated for other images. To test this, we applied the correction models to a new batch of images (5
467 TM, 3 ETM-H, and 2 ETM-L) and the results confirm that the error is corrected in a similar manner.
468 Therefore, the standard deviation obtained with 5 TM images with which the model was made was 5.7 m
469 and the standard deviation obtained with the confirmation images was 5.1 m. A similar result was
470 obtained with the ETM-H images (with a mean standard deviation of 5.2 m for the images used in
471 defining the model and 5.3 m for the confirmation images) and ETM-L (6.4 m average for the images
472 used to define the equation and 5.8 for the confirmation images).

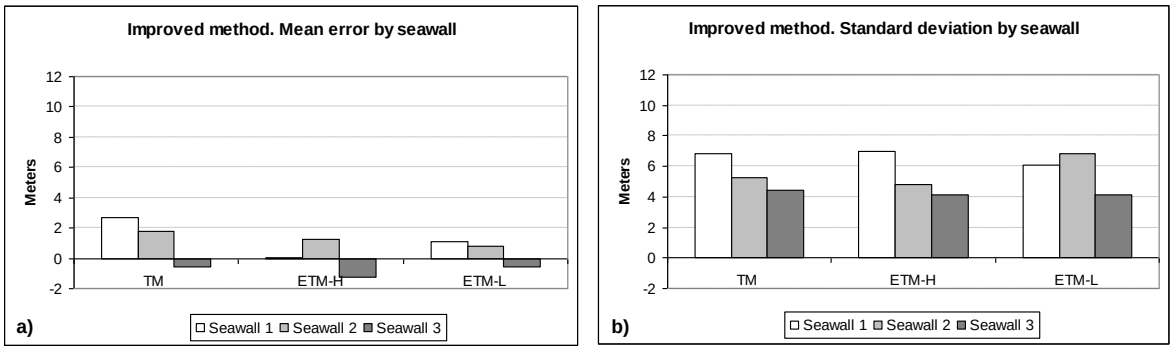


473

474 *Fig. 12. Mean error (a) and standard deviation (b) of the errors for each of the evaluation zones.*

475

476 It is also worthwhile analysing the responses for the three studied seawalls. Figure 12a shows the mean
477 errors obtained near each seawall for each of the image types after the correction was applied, and Figure
478 12b shows the standard deviations. When comparison is made with the results shown in Figure 8, it can
479 be seen that the systematic error on Seawall 2 has disappeared. In fact, it is now at Seawall 1 where we
480 find the greatest errors because of the unique curves in the shoreline at this sector. This differentiation can
481 be seen more clearly in the TM and ETM-H images. In the case of ETM-L, the correction has been less
482 efficient and is less evident. In fact, in these images the maximum standard error deviation can be seen in
483 Seawall 2.

484

485 # 7. Determination of the accuracy of the proposed method

486 To determine the potential use of the shorelines extracted with the proposed method it is necessary to
487 establish the fundamental limits of error. With this intention the sample was expanded for each type of
488 image and error analyses in the control zone were made on 28 TM images, 10 ETM-H images, and 7
489 ETM-L images, or a total of 45 images from various dates (Fig. 13).

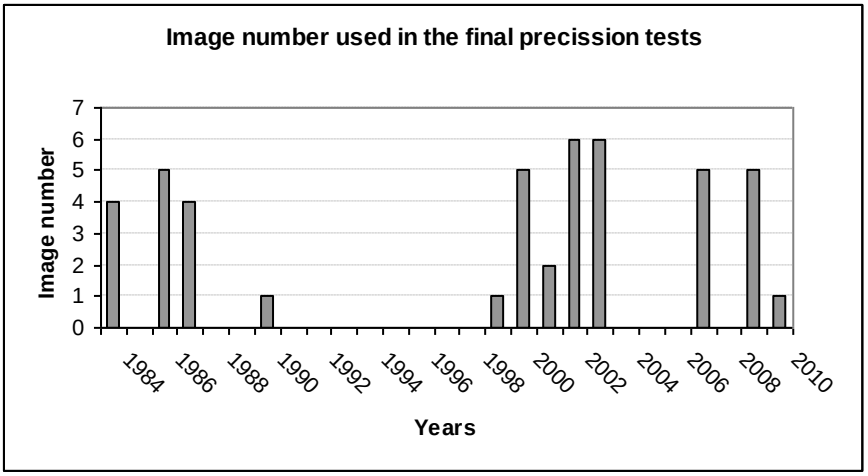


490

491 Figure 13. Number of images per year analysed to assess levels of precision using the developed method.

492

493 Once the data set with the error magnitudes is collated it can be observed that the errors follow an
494 approximately normal distribution (Fig. 14). The Kolmogorov-Smirnov test was applied and it was found
495 that the distribution fits a normal curve with a confidence level of 95%. Accordingly, this distribution was
496 used to determine the likely maximum error that could occur for each type of image. Table 5 shows the

mean error for each image type, ranging between -1.22 and -1.63, i.e. values close to zero but with a very small landward bias. The standard error deviation is also shown and since the mean error is very close to zero, the RMSE is used. It can be seen that in all cases it is very close to 5 m. From the adjustment distance to a normal curve the maximum error potential towards the sea or land was determined with three levels of confidence: for ETM-H images the maximum error in the position of the shoreline at one time may be, with 90% probability, 10.54 m (calculated by adding the maximum landward and seaward error with that level of confidence); with TM images the maximum error is 11.09 m; and with ETM-L images the maximum error is 13.24.

This level of precision is good given that we are using images with a resolution of 30 m.

*Table 5. Basic error statistics obtained from analysis of 45 Landsat TM and ETM images of Seawalls 2 and 3 in the study area. For each type of image the following information is given: the period when the image was taken; the number of images analysed; the number of points from which errors have been measured; the mean error for the whole sample (the negative value indicates that error is towards the land); the mean square error; and maximum errors to be expected with various confidence levels (shown in brackets).*

| Image type | TM | ETM-H | ETM-L |
|---|---|---|---|
| Number of analysed images | 28 | 10 | 7 |
| No. points used | 26109 | 9230 | 6651 |
| Mean error (m) | -1.66 | -1.57 | -1.22 |
| RMSE (m) | 4.96 | 4.69 | 5.47 |
| Max. seaward error (m) [99 %] | 9.91 | 9.34 | 11.51 |
| Max. landward error (m) [99 %] | 11.57 | 11.00 | 13.17 |
| Max. seaward error (m) [95 %] | 6.52 | 6.14 | 7.78 |
| Max. landward error (m) [95 %] | 8.18 | 7.80 | 9.44 |
| Max. seaward error (m) [90 %] | 4.71 | 4.44 | 5.79 |
| Max. landward error (m) [90 %] | 6.37 | 6.10 | 7.45 |

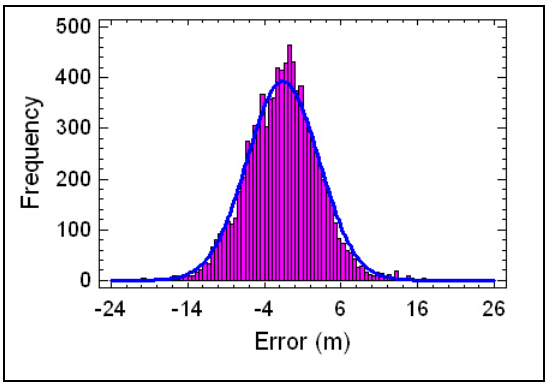

*Fig. 14. Histogram of the frequency of errors found on ETM-H images and tracing the normal adjusted curve.*

## 8. Discussion and conclusions

We have developed a method to automatically extract the position of the shoreline from successive Landsat TM and ETM+ images with subpixel precision. This has been achieved by applying an algorithm to automatically extract the shoreline – as well as a system of subpixel geo-referencing. Correction has been added for the effect caused by differences in radiometric levels in the land area. We assessed the accuracy of the method of extracting the shoreline from 45 Landsat TM and ETM+ images taken between 1984 and 2010 in two coastal segments of 2.4 and 2.7 km. These segments of shoreline had been stabilised artificially by seawalls throughout the study period and comparisons were made with the position extracted manually from aerial photos taken with a spatial resolution of 0.5 m. By analysing each of the 41,990 automatically extracted points we have been able to calculate the statistical parameters of the error. The RMSE is around 5 m and the mean error is about -1.5 m.

Given these results, what types of change can we expect to recognise in shorelines calculated with this method on microtidal coasts such as found in the Mediterranean? Firstly, this method can be used to measure erosion or accumulation trends in beaches over the medium and long term. Note that given the configuration of the errors (Fig. 14) the method usually locates the position of the shoreline with great precision. For example, the error obtained with a probability of 75% would range between 1.7 m seaward and 3.36 m landward. Therefore, most of the shorelines extracted reveal a high level of metric accuracy. In any case, it is also important to note that the main advantage of this application is that many lines can be drawn automatically. While accepting that some segments will be described with less precision it is clear that trends are defined without difficulty. Note, for example, that while the control area has been analysed using only images available on the USGS server, we have been able to use up to 45 different images recorded between 1984 and 2010.

Another important issue is whether seasonal variability in the width of beaches on seas without tides can be derived from the data obtained. The coast in the study area has an average annual maximum sea level oscillation of 0.37 m and large sections of the beaches are gently sloped. Monitoring a segment of 9 km of beach at El Saler, south of Valencia, over the past five years has shown that the average beachface slope

544 is 3.7º (Pardo-Pascual *et al.*, 2011). We can calculate that the movements of the shore due exclusively to
545 factors related to the level of the sea measure about 5.7 m. The RMSE of the presented method – even for
546 the worst performing ETM-L images – is better than the average oscillation of the shore due to changes in
547 sea level – and therefore the precision achieved is sufficient for seasonal variability studies. The
548 application of this tool may enable various positions of the shore to be identified in the same area during
549 the period of a year. In fact, this study employs up to six images for each of the years 2002 and 2003.

550 Another important question is whether this type of application could be used to calculate positions of the
551 shoreline on macrotidal coasts. In the current state of development it is difficult to determine if the
552 precision demonstrated could be repeated for tidal coasts. We have seen how differences in spectral
553 response in areas near the coast clearly influence calculations regarding the position of the shoreline. The
554 fact that a large landward area immediately adjacent to the water line appears wet can significantly alter
555 the response of the algorithm that determines the shoreline. It would be necessary to establish which
556 spectral region would be the most efficient in adequately determining the position. Ryu *et al.* (2002)
557 showed that a coastline with tidal flows can be determined using NIR bands, however it was reported that
558 this approach does not work well when the water is in a state of reflux – this is because of the confusion
559 caused by the existence of wet areas immediately beside the shore. In any event, it remains to be
560 confirmed to what extent the methodology outlined here could help calculate the shoreline in areas with
561 large tides. Moreover, it has to be remembered that the complexity of determining the accuracy with
562 which a shoreline is determined is further complicated by the very vagueness of the concept of a shoreline
563 in areas with tides – as stated in the introduction.

564 It is therefore concluded that in microtidal coastlines the shorelines obtained from Landsat TM and ETM+
565 images using the procedure described can be used to map intranual variability in the shoreline (since
566 small changes can be recognised), as well as to quantify local erosion and /or accumulation trends in the
567 medium term. Therefore, this may be a useful tool for the management of coastal areas. Because the
568 whole process can be automated, the use of this methodology in the management of coastal areas may be
569 both simple and efficient.
570
571
572
573

## 9. Acknowledgements

The authors appreciate the financial support provided by the Spanish *Ministerio de Ciencia e Innovación* and the Spanish *Plan E* in the framework of the Projects CGL2009-14220-C02-01 and CGL2010-19591.

## 10. References

Bayram, B., Acar, U. & Ari, A. (2008): A novel algorithm for coastline fitting through a case study over the Bosphorus, *Journal of Coastal Research*, 24 (4): 938-991.

Boak, E.H. & Tunner, I.L. (2005): Shoreline definition and detection: a review, *Journal of Coastal Research* 21 (4): 688-703.

Braud, D.H. & Feng, W. (1998): *Semi-automaed construction of the Lousiana coastline digital land/water boundary using Landsat Thematic Mapper satellite imagery*, Departament of Geography & Anthropology, Lousiana State University, Lousiana Applied Oil Spill Research and Development Program, OSTAPD Technical Report Series 97-002.

Brocal, R., López-García, M.J. & Pardo-Pascual, J.E. (2001): Cambios en la línea de costa mediante fotografía aérea e imágenes IRS-Pan en el litoral valenciano: sector Cullera-Tavernes (1956-1999), en J.I. Rosell & J.A. Martínez-Casanovas (eds.) *Teledetección. Medio Abmiente y Cambio Global*, Universitat de Lleida, pp. 225-228.

Brocal, R., López-García, M.J. & Pardo-Pascual, J.E. (2005): Análisis de la evolución de la línea de costa enel litoral valenciano mediante SIE e imágenes de satélite, El sector Cullera-Tavernes (1956-1999), en E. Sanjaume & J.F. Mateu (eds.): *Geomorfologia litoral i quaternari. Homenatge al professor Vicenç Mª Rosselló i Verger*, Publicacions de la Universitat de València, pp. 73-86.

Chu, Z.X., Sun, X.G., Zhai S.K. & Xu, K.H. (2006): Changing pattern of accretion/erosion of the modern Yellow River (Huanghe) subaerial delta, China: Based on remote sensing images, *Marine Geology*, 227: 13– 30.

DGC, Spanish Coastal General Office (2008): *Directrices sobre actuaciones en playas*, Secretaria general para el Territorio y la Biodiversidad, Dirección General de Costas, Ministerio de Medio Ambiente de España 41 pp. In http://www.mma.es/secciones/acm/aguas_marinas_litoral/directrices/pdf/directrices_sobre_playas.pdf

Di, D., Ma, R. & Li.R. (2003b): Geometric processing of Ikonos stereo imagery for coastal mapping applications, *Photogrammetric Engineering & Remote Sensing*, 69 (8): 873-879.

Di, D., Wang, J., Ma, R. & Li.R. (2003a): Automatic shoreline extraction from high-resolution Ikonos satellite imagery, *ASPRS 2003Annual Conference Proceedings*, Anchorage, Alaska.

Ekercin, S. (2007): Coastline change assessment at the Aegena Sea Coasts in Turkey using multitemporal Landsat imagery, *Journal of Coastal Research* 23 (3): 691-698.

610 Espinosa Montero, V. & Rodríguez Santalla, I (2009): Evolución costera del tramo comprendido entre
611 San Juan de los Terreros y playas de Vera (Almería), *Revista de la Sociedad Geológica de*
612 *España* 22 (1-2): 3-12.

613 Foody, G.M., Muslim, A.M. & Atkinson, P. M. (2005): Super-resolution maping of the waterline frfom
614 remotely sensed data, *International Journal of Remote Sensing*, 24: 5381-5392.

615 Frazier, P.S. & Page, K.J., (2000): Water body detection and delineation with Landsat TM data,
616 *Photogrammetric Engineering & Remote Sensing*, 66 (12): 1461-1467.

617 Gens, R. (2010): Remote sensing of the coastlines: detections, extraction & monitoring, *International*
618 *Journal of Remote Sensing*, 31 (7): 1819-1836.

619 Guariglia, A., Buonamassa, A., Losurdo, A., Saladino, R., Trivigno, M.L., Zaccagnino, A. & Colangelo,
620 A. (2006): A multisource approach for coastline mapping & identification of the shoreline
621 changes, *Annals of Geophysics*, 49 (1): 295-304.

622 Guizar-Sicairos, M., Thurman, S.T. & Fienup, J.R. (2008): Efficient subpixel image registration algorithms,
623 *Optics Letters*, 33 (2): 156-158.

624 Hoeke, R.K., Zarrillo, G.A. & Synder, M. (2001): *A GIS based tool for extracting shorelines positions*
625 *forma aerial imagery (BEACHTOOLS)* Coastal Engineering Technical Note IV, Washington
626 DC: US Army Corps of Engineers, 12 p.

627 Jiménez, J.A., Sánchez-Arcilla, A., Bou, J. & Ortiz, M.A. (1997): Analysis short-term shoreline changes
628 along the Ebro Delta (Spain) using aerial photographs, *Journal of Coastal Research* 13 (4):
629 1256-1266.

630 Jishuang, Q & Chao, W. (2002): A multi-thershold based mnorphological approach for extractin coastal
631 line feature in remote sensed images, Pecora 15/L& Satellie Information IV Conference (Denver,
632 Colorado), ISPRS Comission I/ FIEOS pp. 319-338.

633 Leatherman, S.P. (1983): Historical and projected shoreline mapping, *Proceedings of the Coastal*
634 *Zone'83* (San Diego, California), pp. 2902-2910.

635 Lee, J.S. & Jurkevich, I. (1990): Coastal detection and tracing in SAR images, *IEEE Transactions on*
636 *Geoscience and Remote Sensing* 28: 662-668.

637 Lisitzin, E. (1974): *Sea level changes.* Oceanography Series 8, Elsevier, Amsterdam, 286 pp.

638 Liu, H., Sherman, D. & Gu, S. (2007): Automated extraction of shorelines from airbone light detection
639 and ranging data and accuracy assessment based on Monte Carlo simulation, *Journal of Coastal*
640 *Research* 23 (6): 1359-1369.

641 Maiti, S. & Bhattacharya, A.K. (2009): Shoreline change analysis and its application to prediction: a
642 remote sensing and statistics based approach. *Marine Geology* 57: 11–23

643 Manavalan, P., Sathyanath, P. & Rajegowda, G.I. (1997): Digital image analysis techniques to estimate
644 waterspread for capacity evaluation of reservoirs, *Photogrammetric Engineering & Remote*
645 *Sensing*, 59 (9): 1389-1395.

646 Mason,D.C. & Davenport, I.J. (1996): Accurate & efficient determination of the shorelinte in ERS-1 SAR
647 images, *IEEE Transactions on Geoscience & Remote Sensing*, 34: 1243-1253.

648 McCurdy, P.G. (1950): Coastal deliniation from aerial photographs, *Photogrammetric Enginnering*, 16
649 (4), 550-555.

650 MOPU, Ministerio de Obras Pùblicas y Urbanismo (1979): *Estudio de la dinámica litoral en la costa*
651 *peninsular mediterránea y onubense. Provincias de Valencia, Castellón y Tarragona*,
652 Laboratorio de Puertos Ramón Iribarren, Dirección General de Costas.

653 Morton, R.A., Miller, T. & Moore, L. (2005): Historical shoreline changes along the US Gulf of Mexico:
654 a summary of recent shoreline comparisons and analyses, *Journal of Coastal Research*21 (4):
655 704-709.

656 Muslim, A.M., Foody, G.M. & Atkinson, P.M. (2006): Localized soft classification for super‐resolution
657 mapping of the shoreline, *International Journal of Remote Sensing*, 27, (11): 2271-2285.

658 Muslim, A.M., Foody, G.M. & Atkinson, P.M. (2007): Shoreline Mapping from Coarse-Spatial
659 Resolution Remote Sensing Imagery of Seberang Takir, Malaysia, *Journal of Coastal Research*,
660 23 (6):1399-1408.

661 NASA (2006): *Landsat 7 Science Data Users Handbook*, (on-line), available on
662 http://landsathandbook.gsfc.nasa.gov/pdfs/Landsat7_Handbook.pdf (September, 2011).

663 Niedermeier, A., Romaneessen, E. & Lehner, S. (2000): Detection of the coastlines in SAR images using
664 wavelet methods, *IEEE Transactions on Geoscience & Remote Sensing* 38: 2270-2281.

665 Ouma, Y.O. & Tateish, R. (2006): A water index for rapid mapping of shoreline changes of five East
666 African Rift Valley lakes: an empirical analysis using Landsat TM & ETM+ data, *International*
667 *Journal of Remote Sensing* 27 (15): 3153-1381.

668 Pardo-Pascual, J.E. & Sanjaume, E. (2001): Análisis multiescalar de la evolución costera, *Cuadernos de*
669 *Geografía*, 69/70: 95-126.

670 Pardo-Pascual, J.E. (1991): *La erosión antrópica en el litoral valenciano,* Conselleria d'Obres Públiques,
671 Urbanisme i Transports, Generalitat Valenciana, 240 pp.

672 Pardo-Pascual, J.E. , Ruiz, L.A., Palomar Vázquez, J., Calaf, X.., Colmenárez, G.R., Almonacid-
673 Caballer, J. & Gracia, G. (2008): Teledetección, GPS y Lidar: Nuevas técnicas de análisis y
674 evolución de la línea de costa y de los espacios playa-duna en Pardo-Pascual, J.E y Ruiz, L.A.
675 (eds.): *Actas de las Jornadas Técnicas "Las nuevas técnicas de información geográfica al*
676 *servicio de la gestión de zonas costeras: Análisis de la evolución de playas y dunas*": 62-68.
677 Servicio Publicaciones UPV.

678 Pardo-Pascual, J.E., Palomar-Vázquez, J.M., García-Asenjo, L. & Garrigues-Talens, P. (2011):
679 Determinación de la tendencia evolutiva de un segmento de playa basándose en múltiples
680 levantamientos tridimensionales, in Montoya, I., Rodríguez-Santalla, I. and Sánchez-García,
681 M.J. (eds.): *Avances en Geomorfología Litoral. Actas de las VI Jornadas de Geomorfología*
682 *Litoral:* 27-30. Ed. Universidad Rey Juan Carlos, Madrid.

683 Pérez-González, L. (2008): La gestión de la costa desde la Administración General del Estado: Lineas de
684 trabajo y perspectivas, en Pardo-Pascual, J.E y Ruiz, L.A. (eds.): *Actas de las Jornadas Técnicas*
685 *"Las nuevas técnicas de información geográfica al servicio de la gestión de zonas costeras:*
686 *Análisis de la evolución de playas y dunas*": 44-48. Servicio Publicaciones Universitat
687 Politècnica de València.

688 Puertos del Estado, *Spanish State Port Authority* (2009): *Remar red de mareógrafos de puertos del estado*
689 *(Informe Anual 2009),* 395 pp. Available on
690 http://w3.puertos.es/export/download/oceanografia_mareografos_informes/infredmar2009.pdf
691 (September, 2011).

692 Pugh, D. (1996): *Tides, surges & mean sea level,* John Wiley & Sons, 472 pp.

693 Pugh, D.T. (2004): *Changing sea levels. Effects of tides, weather and climate.* Cambridge University
694 Press, 280 pp.

695 Robertson, W.V., Whitman, D., Zhang, K.Q. & Leatherman, S.P. (2004): Mapping shoreline position
696 using airborne laser altimetry, *Journal of Coastal Research,* 20 (3): 884-892.

697 Rodríguez, I. (2001): Comparación de técnicas basadas en el tratamiento digital de imágenes de satélite
698 para la obtención de la línea de costa del Delta del Ebro, en J.I. Rosell & J.A. Martínez-
699 Casanovas (eds.) *Teledetección. Medio Abmiente y Cambio Global,* Universitat de Lleida. Pp.
700 205-208.

701 Rodríguez, I., Sánchez, M.J. & Montoya, I. (2009): Estudios de erosión con satélite en costas
702 sedimentarias micromareales, *en* J. Alcántara Carrió, I.D. Correa Arango, F.I. Isla Mendy, M.
703 Alvarado Ortega, A.H.F. Klein, A. Cabrera Hernández y R. S&oval Barlow (Eds). *Métodos en*
704 *Teledetección Aplicada a la Prevención de Riesgos Naturales en el Litoral*. Servicio de
705 Publicaciones del Programa Iberoamericano de Ciencia y Tecnología para el Desarrollo, pp. 65-
706 78.

707 Ruiz, L.A., Pardo-Pascual, J.E., Almonacid-Caballer, J.& Rodríguez, B. (2007): Coastline automated
708 detection and multi-resolution evaluation using satellite images. *Proceedings of Coastal Zone*
709 *2007*, 22 - 26 July, Portland.

710 Ryu,J-H, Won, J-S, Min, K.M. (2002): Waterline extraction from Landsat TM data in a tidal flat: A case
711 study in Gomso Bay, Korea *Remote Sensing of Environment* , 83 (3): 442-456.

712 Sanjaume, E. & Pardo-Pascual, J.E. (2005): Erosion by human impact on the Valencian costline, *Journal*
713 *of Coastal Research,* SI 49: 76-82.

714 Sanjaume, E. (1985): *Las costas valencianas. Sedimentología y morfología*, Universitat de València, 505
715 p.

716 Sanjaume, E. Rosselló, V. Pardo-Pascual, J.E., Carmona, P. López, M. & Segura, F. (1996): Recent
717 coastal changes in the Gulf of Valencia (Spain), *Zeitschrift für Geomorphologie,*
718 *Supplementbände,* 102: 95-118.

719 Serra-Peris, J. (1986): 'Procesos litorales en la costa de Castellón', PhD Thesis, Escuela Técnica Superior
720 de Ingenieros de Caminos, Canales y Puertos, Universidad Politécnica de Valencia, 891 p.

721 Smith, G.L. & Zarrillo, G.A. (1990): Calculating long-term shoreline recession rates using aerial
722 photographic and beach profiling techniques, *Journal of Coastal Research* 6 (1): 111-120

723 Stafford, D.B. (1971): *An aerial photographic technique for beach erosion surveys in North Carolina,*
724 U.S. Army Coastal Engineering Research Center, Technical Memorandum, Nº 36, 115 pp.

725 Stockdon, H.F., Sallenger, A.H., List, J.H. & Holman, R.A. (2002): Estimation of the shoreline position
726 and change using airborn topographic lidar data, *Journal of Coastal Research*, 18 (3): 502-513.

727 Thieler, E.R. & Danforth, W.W. (1994): Historical shoreline mapping (I): improving techniques and
728 reducing positioning errors, *Journal of Coastal Research* 10 (3): 549-563.

729 White, K & El Asmar, H. (1999): Monitoring changing position of coastlines using Thematic Mapper
730 imagery, and example from the Nile Delta, *Geomorphology,* 29: 93-105.

731 White, S.A. & Wang, Y. (2003): Utilizing DEMs derived from LIDAR data to analyze morphologic
732 change in the North Carolina coastline, *Remote Sensing of the Environment*, 85: 39-47.

Yamayo, H., Shimazaki, H., Matsunaga, T., Ishoda, A., McClennen, C., Yokoki, H. Fujita, K., Osawa, Y. & Kayanne, H. (2006): Evaluation of various satellite sensors for waterline extraction in a coral reef environment: Majuro Atoll, Marshall Islands, *Geomorphology*, 82: 398-411.

Yu, Y. & Acton, S.T. (2004): Automated delineation of coastline from polarimetric SAR imagery, *International Journal of Remote Sensing*, 25: 3423-3438.

## List of figures

Figure 1. Seawalls in the study area.

Figure 2. The figure illustrates the scheme of the first phase: an approximation of the positioning of the coast at pixel level.

Figure 3. Basic scheme of the calculation procedure for the shoreline position: a) the neighbouring pixels of the approximate line are selected; b) resampling is performed to produce a greater density of points for the mathematical function; c) the function and its line of inflection is mathematically obtained.

Figure 4. Approximate line at pixel level (in blue); the green crosses show the calculations made for each analysed profile; and the pink line indicates the averaged position of the multiple solutions determined by the various profiles and the calculated shoreline.

Figure 5. Example of the result for a segment of shoreline that has been artificially stabilised. Yellow dots show the position of the shoreline image obtained from Landsat 5 (2000-03-01). The red line shows the reference shoreline taken from the aerial photo with an underlying resolution of 0.5 m.

Fig. 6. Mean error (a) and standard deviation detected (b) expressed in meters for each image according to the date when the image was taken and type of image.

Fig. 7 Examples of error. In (a) it can be seen that there are two families of shorelines (see explanation in the text) that appear to be related to a change in the landscape that significantly affected the intensity value (IV) the land. In (b) it can be seen that in this sector for all of the period studied the error was homogenous and the variability between the 23 shorelines was minimal.

Fig. 8 Mean error (a) and standard deviation (b) for each of the three seawalls

Fig. 9. Example of localisation around Seawall 1. Evidence from these results suggests that the mathematical model for the extraction of the shoreline based on Landsat images usually works fairly well. However, errors are produced that seem to be directly related to the characteristics of the digital levels with which the extraction algorithm operates – meaning the 7 x 7 pixel neighbourhood.

Fig. 10 (a) Relationship between the mean pixel intensity considered in the analysis and the error in the positioning of the shoreline in areas near seawalls. (b) shows the relationship between the standard deviation of the pixel intensity values in the analysis and errors. In both cases, the relationship shown is found on the 199-032 series of images taken by the ETM + high gain sensor (21 July 1999).

Fig. 11. Mean error and standard deviation of the error after applying the improved method.

*Fig. 12. Mean error (a) and standard deviation (b) of the errors for each of the evaluation zones.*

Figure 13. Number of images per year analysed to assess levels of precision using the developed method.

*Fig. 14. Histogram of the frequency of errors found on ETM-H images and tracing the normal adjusted curve.*

## List of tables

Table 1. Characteristics of images analysed. The image type column distinguishes between images taken by the TM sensor and those taken with the ETM high gain (ETM-H) and ETM low gain (ETM-L).

Table 2. Shows the application of subpixel geometric correction and a summary of errors found after applying the geometric correction and the algorithm to Landsat images. The error values are in meters. Columns d (*x*) and d (*y*) show the displacement in *xy* applied after geometric correction.

Table 3. Basic statistics of the models obtained for the three types of images

Table 4. Comparison of errors when using the algorithm in its original form and with the improvements after correcting for the effect associated with the characteristics of the image. The column *Model* indicates whether the image was used or not to define the applied correction models.

Table 5. Basic error statistics obtained from analysis of 45 Landsat TM and ETM images of Seawalls 2 and 3 in the study area. For each type of image the following information is given: the period when the image was taken; the number of images analysed; the number of points from which errors have been measured; the mean error for the whole sample (the negative value indicates that error is towards the land); the mean square error; and maximum errors to be expected with various confidence levels (shown in brackets).

**Figure 1**

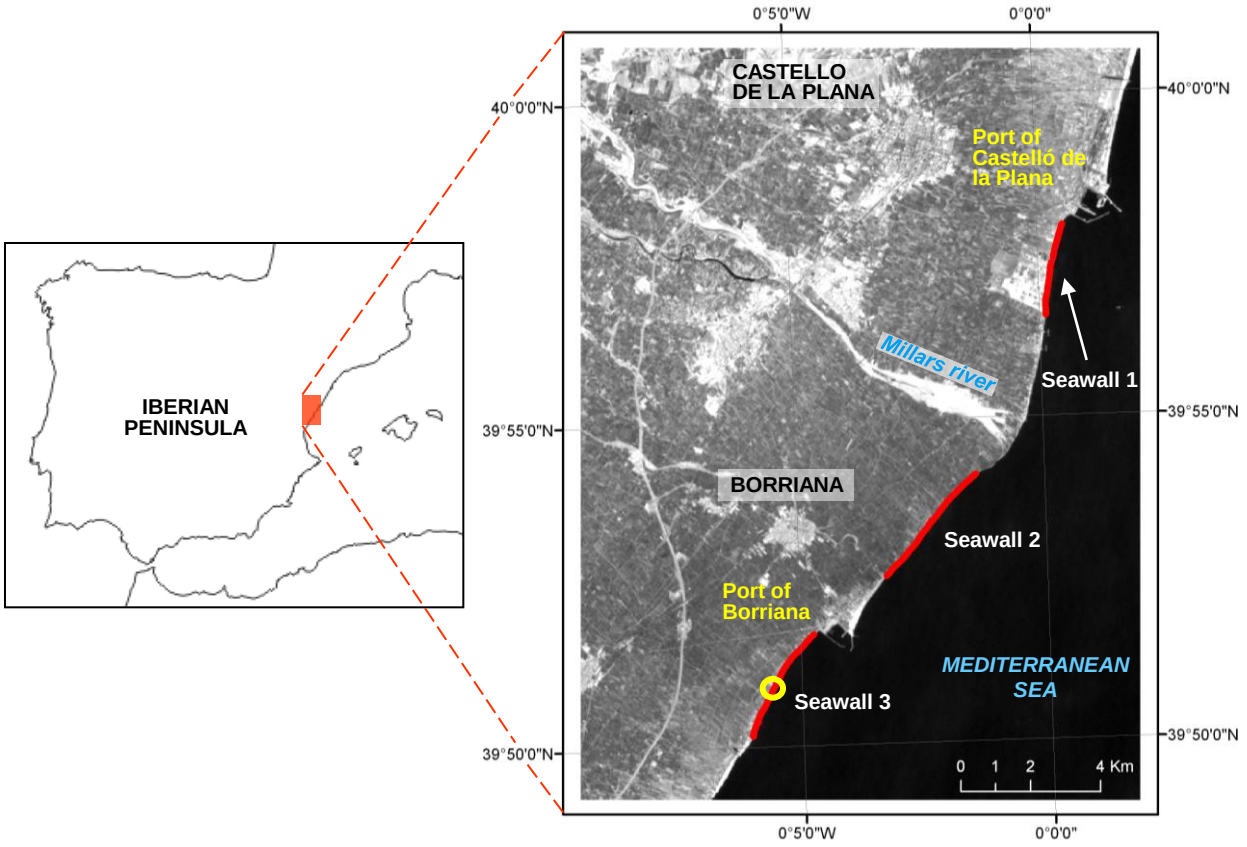
IBERIAN
PENINSULA
0°5'0"W
0°0'0"
40°0'0"N
39°55'0"N
39°50'0"N
CASTELLO
DE LA PLANA
Port of
Castelló de
la Plana
Millars river
Seawall 1
BORRIANA
Seawall 2
Port of
Borriana
MEDITERRANEAN
SEA
Seawall 3
0 1 2 4 Km

**Figure 2**

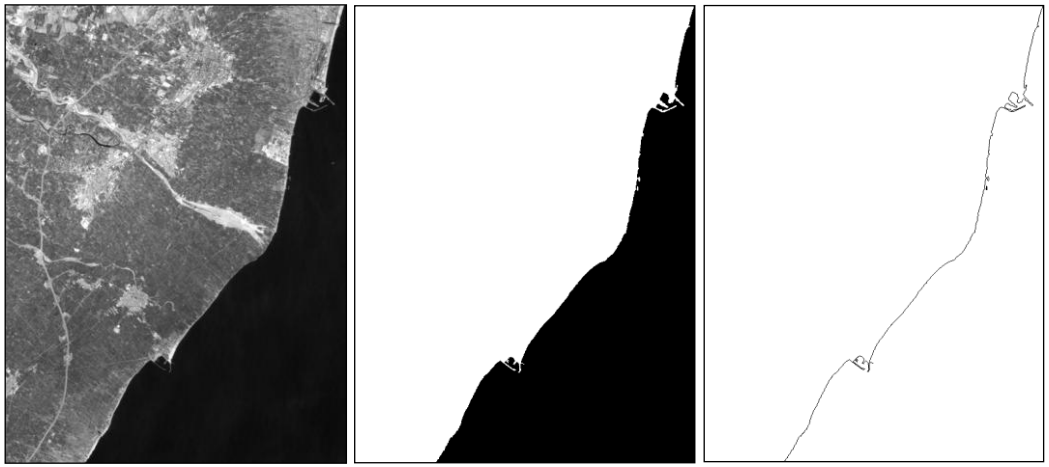

**Figure 3**

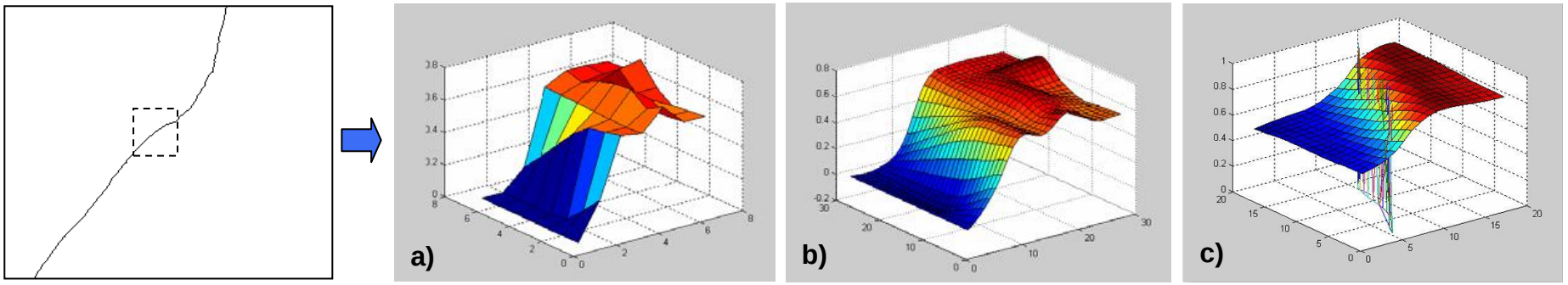

**Figure 4**

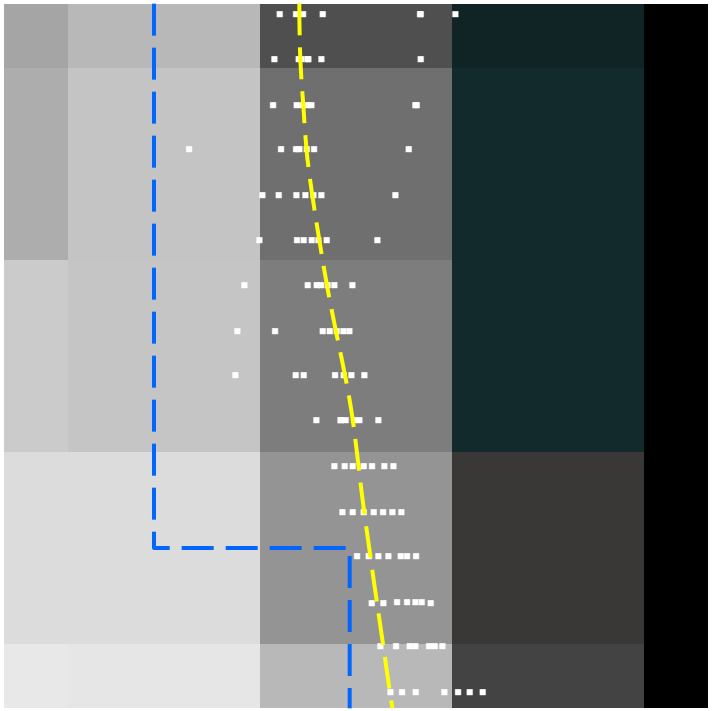

**Figure 5**

**Figure 6**

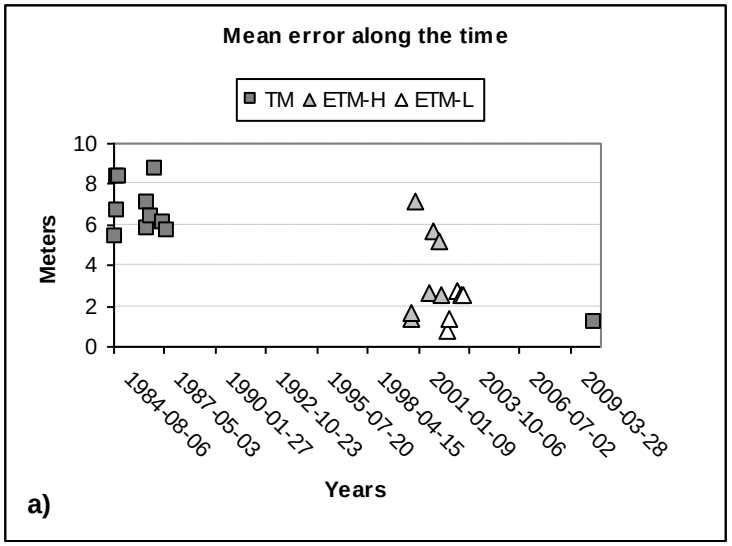
Mean error along the time
TM ETM-H ETM-L
Meters
10
8
6
4
2
0
1984-08-06
1987-05-03
1990-01-27
1992-10-23
1995-07-20
1998-04-15
2001-01-09
2003-10-06
2006-07-02
2009-03-28
Years
a)

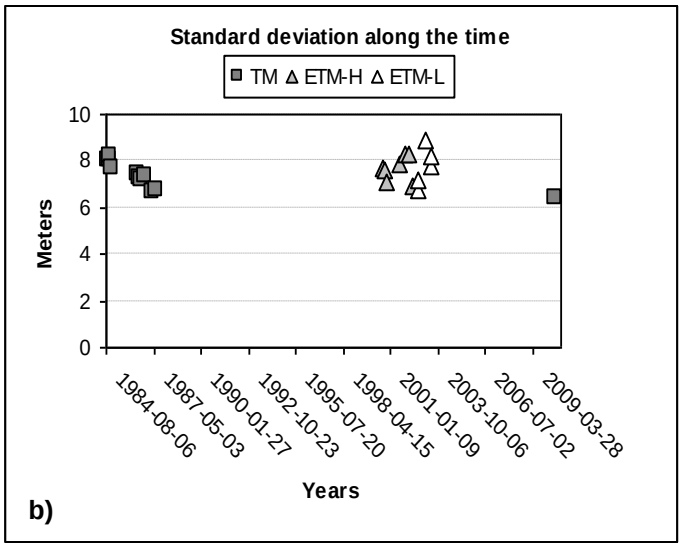
Standard deviation along the time
TM ETM-H ETM-L
Meters
10
8
6
4
2
0
1984-08-06
1987-05-03
1990-01-27
1992-10-23
1995-07-20
1998-04-15
2001-01-09
2003-10-06
2006-07-02
2009-03-28
Years
b)

**Figure 7**

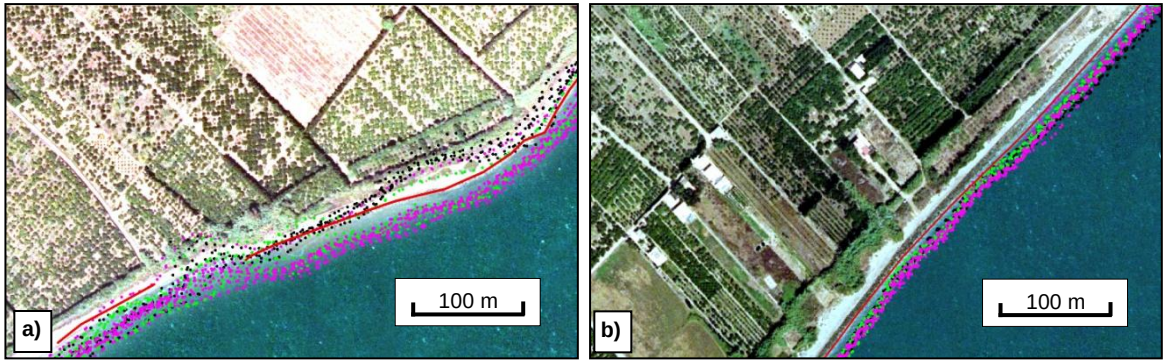

**Figure 8**

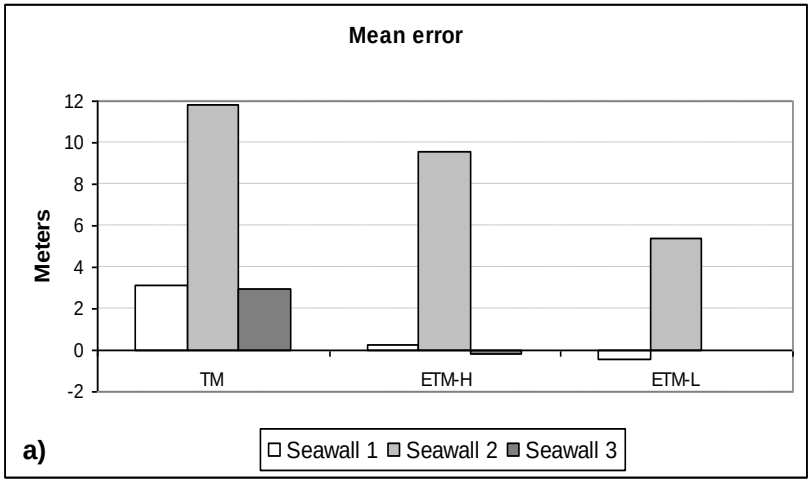
Mean error
Meters
12
10
8
6
4
2
0
-2
TM
ETM-H
ETM-L
a)
Seawall 1
Seawall 2
Seawall 3

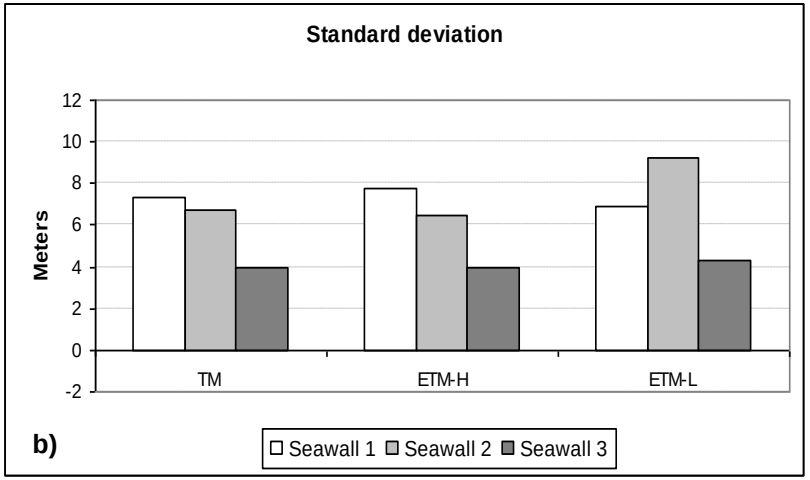
Standard deviation
Meters
12
10
8
6
4
2
0
-2
TM
ETM-H
ETM-L
b)
Seawall 1
Seawall 2
Seawall 3

**Figure 9**

**Figure 10**

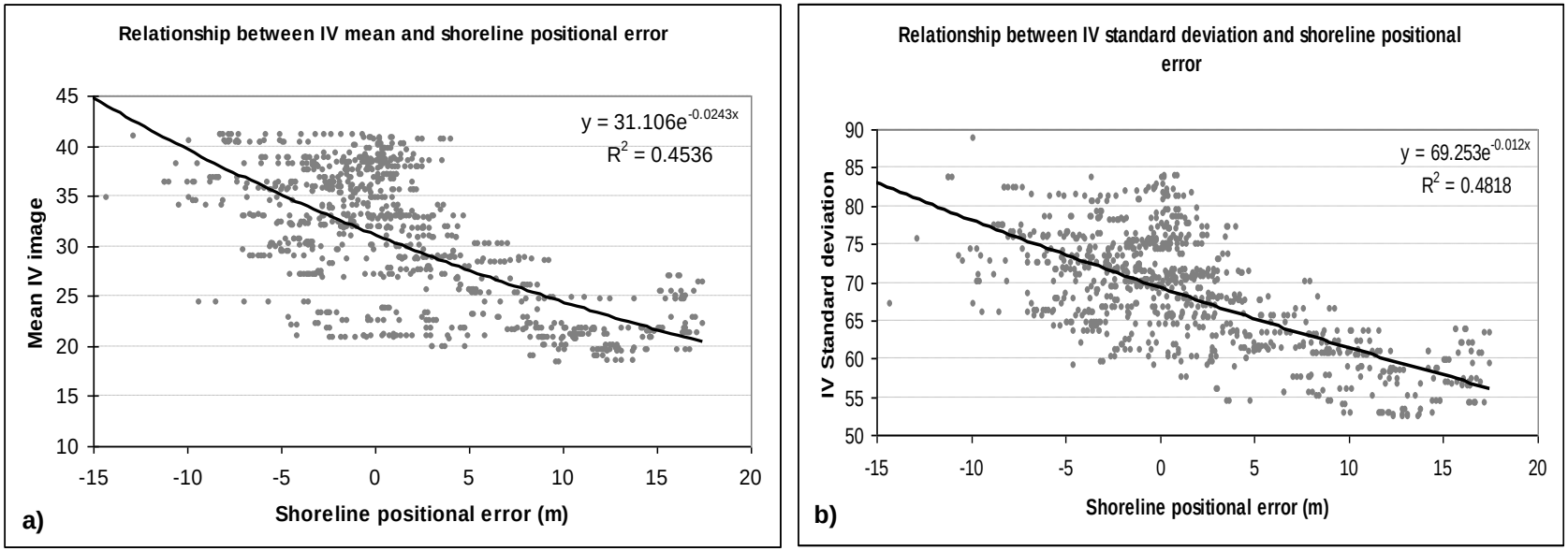
Relationship between IV mean and shoreline positional error
y = 31.106e-0.0243x
R2 = 0.4536
Mean IV image
Shoreline positional error (m)
a)
Relationship between IV standard deviation and shoreline positional error
y = 69.253e-0.012x
R2 = 0.4818
IV Standard deviation
Shoreline positional error (m)
b)

**Figure 11**

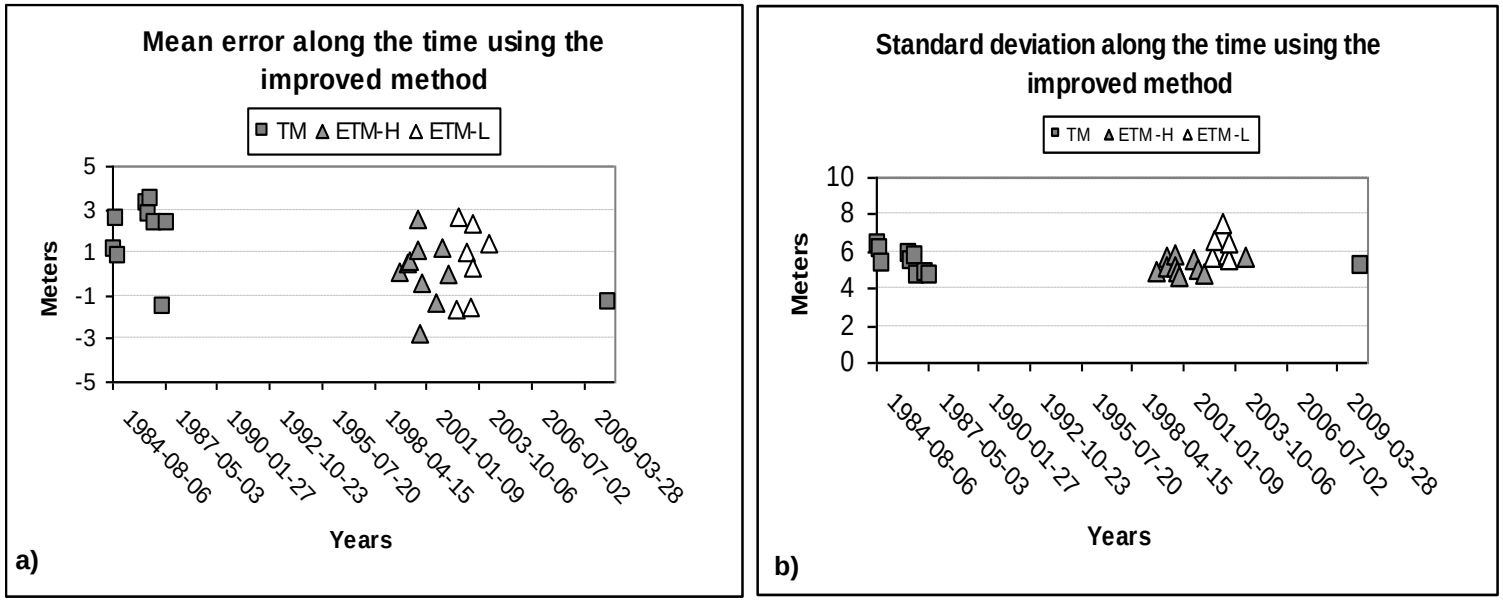
Mean error along the time using the improved method
TM ETM-H ETM-L
Meters
5
3
1
-1
-3
-5
1984-08-06
1987-05-03
1990-01-27
1992-10-23
1995-07-20
1998-04-15
2001-01-09
2003-10-06
2006-07-02
2009-03-28
Years
a)
Standard deviation along the time using the improved method
TM ETM-H ETM-L
Meters
10
8
6
4
2
0
1984-08-06
1987-05-03
1990-01-27
1992-10-23
1995-07-20
1998-04-15
2001-01-09
2003-10-06
2006-07-02
2009-03-28
Years
b)

**Figure 12**

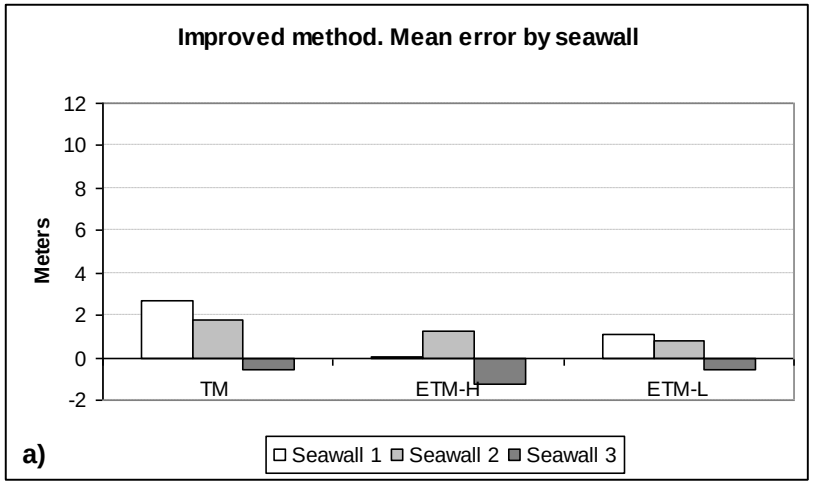
Improved method. Mean error by seawall
Meters
12
10
8
6
4
2
0
-2
TM
ETM-H
ETM-L
a)
Seawall 1
Seawall 2
Seawall 3

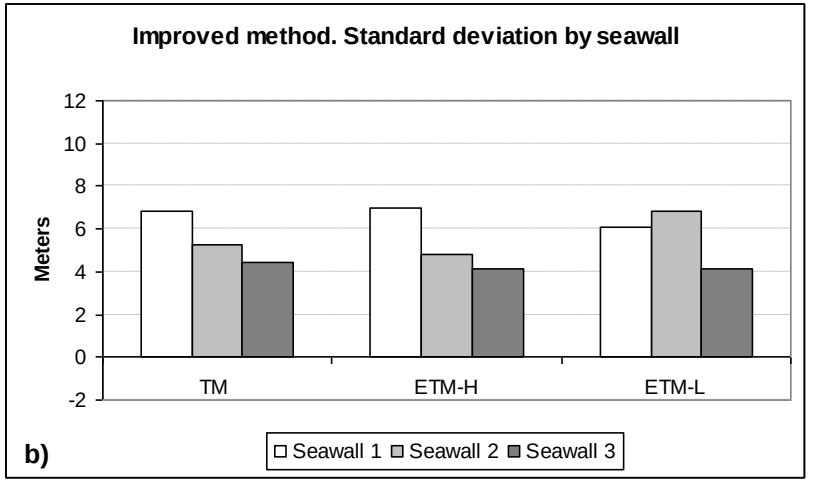
Improved method. Standard deviation by seawall
Meters
12
10
8
6
4
2
0
-2
TM
ETM-H
ETM-L
b)
Seawall 1
Seawall 2
Seawall 3

**Figure13**

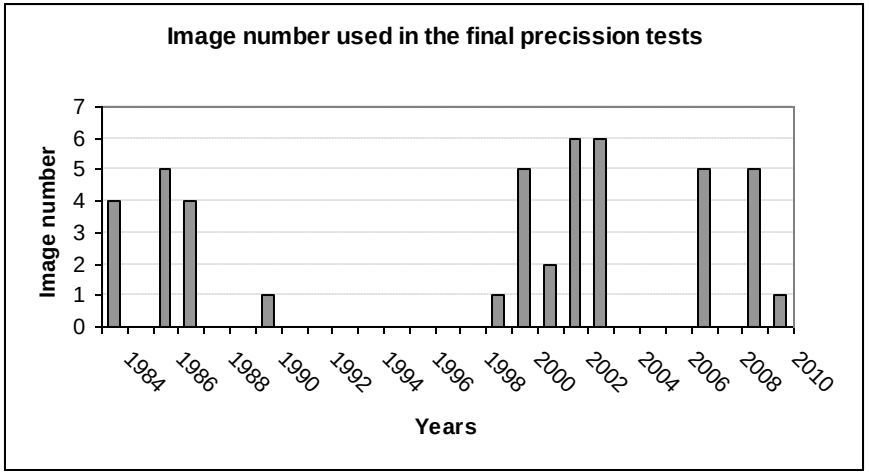
Image number used in the final precission tests
Image number
0
1
2
3
4
5
6
7
1984
1986
1988
1990
1992
1994
1996
1998
2000
2002
2004
2006
2008
2010
Years

**Figure 14**

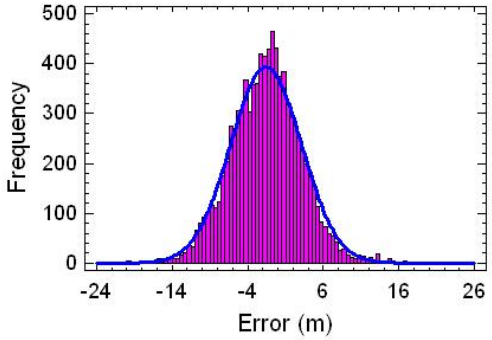

# Automatic Extraction of Shorelines from Landsat TM and ETM+ Multi-Temporal Images with SubPixel Precision

**Josep E. Pardo-Pascual [a*], Jaime Amonacid-Caballer [a], Luis A. Ruiz [a], Jesus Palomar-Vazquez [a]**

*[a]Geo-Environmental Cartography and Remote Sensing Group*
*Department of Cartographic Engineering, Geodesy and Photogrammetry*
*Universitat Politèctica de València.*
*Camí de Vera s/n, 46022 València, Spain*
*Corresponding author. Email: jepardo@cgf.upv.es*
*Phone: 34963877007 (Ext:75537); Fax: 34963877559*

## Abstract

A high geometric precision method for automated shoreline detection from Landsat TM and ETM+ imagery is presented. The methodology is based on the application of an algorithm that ensures accurate image geometric registration, and a new algorithm for sub-pixel shoreline extraction, both at sub-pixel level. The analysis of the initial errors shows the influence of the differences in reflectance of land cover types over the shoreline detection, allowing us to create a model to substantially reduce these errors. Three correction models were defined attending to the type of gain used in the acquisition of the original Landsat images. Error assessment tests were applied on three straight coast segments artificially stabilized, all of them located in microtidal coastal areas. A testing set of 45 images (28 TM, 10 ETM high-gain and 7 ETM low-gain) was used. The mean error obtained in shoreline location ranges from 1.22 to 1.63 m, and the RMSE from 4.69 to 5.47 m. Since the errors follow a normal distribution, then the maximum error at a given probability can be estimated. The results obtained show the possibility to apply this methodology over large coastal sectors in order to determine and analyse the evolution trend of these dynamic areas.

Keywords: shoreline subpixel detection, Landsat images, coastal processes, beach management.

## Acknowledgements

The authors appreciate the financial support provided by the Spanish *Ministerio de Ciencia e Innovación* in the framework of the Projects CGL2009-14220-C02-01 and CGL2010-19591.